Revision 1

Comparative thermal and compressional behaviour of natural xenotime-(Y), chernovite-(Y) and monazite-(Ce)

Francesco Pagliaro[1], Davide Comboni[1,2], Tommaso Battiston[1], Hannes Krüger[3], Clivia Hejny[3], Volker Kahlenberg[3], Lara Gigli[4], Konstantin Glazyrin[5], Hanns-Peter Liermann[5], Gaston Garbarino[2], G. Diego Gatta[1], Paolo Lotti[1*]

[1] Dipartimento di Scienze della Terra, Università degli Studi di Milano, Via Botticelli 23, 20133 Milano, Italy

[2] European Synchrotron Radiation Facility, 71 Avenue des Martyrs, CS 40220, 38043 Grenoble Cedex 9, France

[3] Institut für Mineralogie und Petrographie, Universität Innsbruck, Innrain 52, 6020 Innsbruck, Austria

[4] Elettra Sincrotrone Trieste S.c.P.A., Strada Statale 14 – km 163.5, 34149 Basovizza, Trieste, Italy

[5] Deutsches Elektronen-Synchrotron DESY, Notkestrasse 85, 22607 Hamburg, Germany

* corresponding author: paolo.lotti@unimi.it

Mineralogical Society

This is a 'preproof' accepted article for Mineralogical Magazine. This version may be subject to change during the production process.
DOI: 10.1180/mgm.2024.70

Dedicated to the memory of Dr. Alessandro Guastoni

Revised manuscript submission date: 06/09/2024

https://doi.org/10.1180/mgm.2024.70 Published online by Cambridge University Press

Abstract

ATO_4 compounds are a class of oxides which includes, among others, the rare-earth elements bearing phosphates and arsenates, REEPO_4 and REEAsO_4. In this study, we have investigated the isothermal high-pressure and the isobaric high-temperature behaviour of natural samples of xenotime-(Y) (ideally YPO_4), chernovite-(Y) ($YAsO_4$) and monazite-(Ce) ($CePO_4$) from the hydrothermal veins outcropping at Mt. Cervandone (Western Italian Alps). Experimental data based on *in situ* X-ray diffraction (both single-crystal and powder techniques with conventional or synchrotron radiation) allow to fit the unit-cell volumes and axial thermal and compressional evolution and provide a suite of refined thermo-elastic parameters. A comprehensive analysis of the role played by the crystal chemistry on the thermo-elastic response of these minerals is discussed, along with the description of the main crystal-structural deformation mechanisms for both the zircon (xenotime and chernovite) and monazite (monazite) structural types. Pressure-induced phase transitions of xenotime-(Y) and chernovite-(Y) are discussed and compared with previous literature data, whereas a change in the compressional behaviour of monazite-(Ce) at ~ 18 GPa, involving an increase in the coordination number of the REE-hosting *A* site, is presented and discussed.

Keywords

xenotime, monazite, chernovite, *AT*O_4, pressure, temperature, phase transition, X-ray diffraction

https://doi.org/10.1180/mgm.2024.70 Published online by Cambridge University Press

Introduction

The general formula *ATO*4 is often used in the literature to define ternary inorganic oxides (Vorres, 1962), where *A* and *T* represent two cations, that can be combined with oxygen (and seldom with other anions) into several structural types, including, but not limited to, scheelite, zircon, monazite, fergusonite, baryte, quartz, cristobalite, wolframite and rutile (Fukunaga and Yamaoka, 1979). In the context of the present study, the *A*-site is occupied by a Rare Earth Element (REE: lanthanides and Y), Ca, U and Th, whereas *T* stands for tetrahedrally-coordinated cations (As and P). Concerning the structural types, in this manuscript almost exclusive attention is directed to the zircon and monazite structures, as demonstrated by the four minerals which are subject of this and two previous works (Pagliaro et al., 2022a,b): chernovite-(Y) [nominally $YAsO_4$], xenotime-(Y) [nominally YPO_4], gasparite-(Ce) [nominally $CeAsO_4$] and monazite-(Ce) [nominally $CePO_4$]. The crystal structure of these minerals has been subject of a large number of studies and reviews (*e.g.*, Mooney, 1948; Ni et al., 1995; Boatner, 2002; Finch and Hanchar, 2003 Kolitsch and Holtstam, 2004; Clavier et al., 2011;) and an overview of the monoclinic monazite-type structure and of the tetragonal zircon-type (also known, but occasionally reported as "xenotime-type") is discussed in the next section.

As reported by several authors (Fukunaga and Yamaoka, 1979; Ushakov et al., 2001; Boatner, 2002; Kolitsch and Holtsam, 2004), whether the monazite or the zircon-type structure is stable (within ATO_4 phosphates and arsenates) depends on different factors. Among others, the atomic radii of either the *A*- and *T*-sites play a dominant role. In general, a large size of the *A*-cation promotes the crystallization of the monazite structural type over the zircon one; on the other hand, the larger the *T*-site cation, the more stable is the zircon structure across the REE-series. Within the REE-bearing phosphates, light REE ranging from La to Eu, with larger ionic radii than heavy-REE, are preferentially hosted by the monazite-type structure, whereas heavy-REE, from Tb to Lu, as well as Y and Sc, fit best into the zircon-type structure (Mooney, 1948; Ni et al., 1995; Boatner, 2002; Kolitsch and Holtstam, 2004; Clavier et al., 2011). A similar behaviour has been reported for the $REEAsO_4$ series, although the threshold among the two structures is shifted to smaller *Z* numbers in the lanthanoid series: the monazite-type structure preferentially hosts REE from La to Nd, whereas the REE from Sm to Lu

https://doi.org/10.1180/mgm.2024.70 Published online by Cambridge University Press

(as well as Y and Sc) are hosted by the tetragonal zircon-type crystal structure (e.g. Ushakov et al., 2001; Boatner, 2002).

The REE-bearing phosphates are common accessory minerals in hydrothermal alteration of granitoid rocks that can control the partitioning of Rare Earth Elements, as well as those of uranium and thorium, since they tend to incorporate these elements into their crystal structures (Rapp and Watson, 1986). In addition, due to their much lower tendency to incorporate Pb, they have found large use for geochronological applications (Harrison et al., 2002). Due to their peculiar physical, chemical and optical properties (such as the low solubility in water fluids), REE phosphates are used or have been proposed in several technological applications, *e.g.,* to produce phosphors (de Sousa Filho and Serra, 2009), ceramic coatings (Morgan et al., 1995; Davis et al., 1998), and materials for the safe storage of actinides originating from radioactive waste (Oelkers and Montel, 2008; Orlova and Ojovan, 2019). Consequently, there has been significant interest in studying the behaviour of REE phosphate minerals and their synthetic counterparts under varying pressure and temperature conditions.

Recent reviews have been published by Errandonea (2017) and Strzelecki *et al.* (2024) for monazite- and zircon-type structures, respectively. Tables S1 and S2 (supplementary materials of this paper) provide a comprehensive list of the thermo-elastic parameters published in the literature for several REETO_4 compounds, along with the related bibliographic references. Concerning the response of REETO_4 compounds to high pressure (hereafter H*P*), as general rule it has been postulated that, for a given structural type, the bulk modulus shifts towards lower values as the atomic radius of the *A*- and *T*-sites increases, which has been highlighted by several authors and corroborated by both theoretical (Zhang et al., 2008; Li et al., 2009) and experimental studies (Zhang et al., 2008; Lacomba-Perales et al., 2010; Errandonea et al., 2011). Regarding the thermal behaviour, there is general agreement on the thermal expansion coefficient of the REETO_4, which shows a clear compositional trend: the thermal expansivity increases along with the ionic radii of the *A*-cation, while it reduces if the radius of the *T*-site increases (Subbarao et al., 1990; Perrière et al., 2007; Zhang et al., 2008; Li et al., 2009). Unfortunately, the published values of both the compressibility and thermal expansivity of the studied REETO_4 are not always internally consistent (see Tables S1 and S2), showing a certain degree

https://doi.org/10.1180/mgm.2024.70 Published online by Cambridge University Press

of scattering even for the same compound. In the case of thermal studies, the use of different thermal equations of state further complicates a comparative analysis. Therefore, in this study, we used the linear thermal expansion coefficient, which is commonly used in the literature, although it is not the most accurate model of the thermal elastic response (along with thermal equations of state commonly used in Earth Sciences).

The relative ratio of the *A* and *T* ionic radii not only affects the structure types adopted by a given compound at ambient conditions, but also its pressure stability field and the structural type of the high-pressure polymorphs. Such a relationship is well described by the so-called Bastide diagram (Bastide, 1987), for which one of the most recent graphical representation is reported in Lopez-Solano *et al*. (2010) (Fig. 1, modified). The zircon-type compounds, as xenotime-(Y) and chernovite-(Y) of this study, may transform at high-pressure into monazite-type or scheelite-type polymorphs. Whether a zircon→scheelite or a zircon→monazite→scheelite transformation occurs depends on the reciprocal relations among the ionic radii of the three atoms involved. A large *T*-cation promotes a zircon-to-scheelite phase transition, while a small *T*-cation favors an intermediate monazite-type polymorph. Looking at the *A*-site cation, the larger it is, the more likely is the formation of a monazite polymorph over the scheelite one, "shifting" the stability field to higher pressures. All the studied zircon-type ATO_4 silicates show a zircon-to-scheelite phase transition, with high-pressure Raman and Density Functional Theory calculations suggesting the occurrence of a high-pressure lower symmetry polymorph preserving the zircon structural configuration before the reconstructive phase transition to reidite (Stangarone et al. 2019). The zircon-to-scheelite phase transition has been described for $YAsO_4$ (~8 GPa) and $YCrO_4$ (~4.2 GPa) (Errandonea et al., 2011), as well as YVO_4 (above ~7.5 GPa) (Jayaraman et al., 1987; Wang et al., 2004; Manjón et al., 2010). A comprehensive description of the zircon-to-monazite phase transition in phosphates, including YPO_4 (xenotime) is reported in Hay *et al*. (2013). The relations between monazite and its H*P*-polymorphs again depend upon the reciprocal relations among the *A*, *T* and oxygen ionic radii. The monazite-to-post-baryte phase transition (space group $P2_12_12_1$) has been described for $REEPO_4$ and $REEVO_4$ at increasing pressures with decreasing REE atomic radius (Lacomba-Perales et al., 2010; Ruiz-Fuertes et al., 2016; Errandonea, 2017). On the other hand, monazite-type $LaVO_4$, $PrVO_4$ and

https://doi.org/10.1180/mgm.2024.70 Published online by Cambridge University Press

$NdVO_4$, under compression, undergo a phase transition to a monoclinic $BaWO_4$-II-type structure (Errandonea et al., 2016; Panchal et al., 2017; Marqueño et al., 2021). Eventually, the monazite-to-scheelite transition has been described for the high-pressure polymorphs of YPO_4 and several other REE-free compounds, as $SrCrO_4$ and $CaSeO_4$ (Crichton et al., 2012; Gleissner et al., 2016).

This study, following the research conducted by Pagliaro *et al*. (2022a,b), which includes a detailed crystal chemistry description, focuses on the high-pressure and temperature behaviour of four REE*T*O_4 mineralogical species from the same locality (Mt. Cervandone, Piedmont, Italy).

Based on experimental single-crystal or powder XRD data collected *in situ* (high-*P* or high-*T*) at synchrotron beamlines or in conventional diffraction laboratories, a comparative analysis of the elastic behaviour and structural deformation mechanisms as a function of the crystal chemistry and structure type has been performed. The adoption of up-to-date experimental techniques and crystallographic methods has allowed us to describe a *P*-induced structural re-arrangement peculiar of the monazite structure type, previously reported by Pagliaro *et al*. (2022b) for gasparite-(Ce) and here confirmed also for monazite-(Ce). Such an intermediate structural configuration, implying the increase in the number of oxygen atoms bonded to the *A*-site (from 9 to 10) before the occurrence of the phase transition to the post-baryte type polymorph at higher pressures, has not been reported in earlier literature for monazite-type phosphates.

Crystal structure description

Zircon-type crystal structure

The first studies concerning the crystal structure of zircon date back to the early 20th century and were carried out independently by Vegard (1916, 1926), Binks (1926), Hassel (1926) and Wyckoff and Hendricks (1928), in the framework of the pioneering works about the silicate's structure determination, later gathered by Bragg (1929) in his *Atomic Arrangement in Silicates*. After the first studies on zircon, its structural type has been described in several REE-bearing compounds, including xenotime-(Y) (Vegard, 1927) and the synthetic counterpart of chernovite-(Y), $YAsO_4$ (Strada and Schwendimann, 1934).

https://doi.org/10.1180/mgm.2024.70 Published online by Cambridge University Press

The zircon-type structure is characterized by a tetragonal *I*-centered lattice (space group $I4_1/amd$). The tetragonal zircon-type structure is constructed by infinite chains of polyhedra, developed along the [001] direction (Fig. 2a and 2d), as the result of the connection, along the polyhedral edges, between the eightfold coordinated *A*-site dodecahedron (AO_8 or $REEO_8$) and the TO_4 tetrahedra (Fig. 2c). The AO_8 polyhedron displays two independent *A*-O atomic distances (Fig. 2c), whereas the TO_4 is an undistorted tetrahedron defined by a single *T*-O bond distance. Each chain is in contact with four others on the (001) plane, through connecting edges along an AO_8 unit and the surrounding four (Fig. 2b). The atomic coordinates of the *A*- and *T*-sites are placed in special, fixed positions, both characterized by a $\bar{4}2m$ point symmetry. The oxygen atom is also at a special position (*m*), being its *y* and *z* coordinates the sole refinable parameters.

Monazite-type crystal structure

Parrish (1939), within the first crystallographic studies on monazites, identified its correct space group as $P2_1/n$. The first description of the monazite-type structure has been reported by Mooney (1948), who investigated the La, Ce, Pr and Nd phosphates as part of the Manhattan project and described the REE atomic site in eightfold coordination. The crystal structure of monazite with the REE site in ninefold coordination has been proposed by Ueda (1953, 1967), but with non-reliable average P-O bond lengths of ~1.6 Å. The structure has been later described correctly by Beall *et al.* (1981), Mullica *et al.* (1984) and Ni *et al.* (1995), whereas an exhaustive review of the monazite-structure type has been carried out by Boatner (2002) and then by Clavier *et al.* (2011). The monazite-type structure can be described as made by infinite chains running along the [001] direction (*c*-axis), composed by the alternation of the REE-coordination polyhedra and the *T*-hosting tetrahedra (Fig. 3).

The REE-polyhedron coordination environment has nine corners (oxygen ligands, $REEO_9$, Fig. 3c). According to Mullica *et al.* (1984), the $REEO_9$ polyhedron can be described as an equatorial pentagon (sharing vertices with five TO_4 tetrahedra of five adjacent chains in correspondence of the $O1_b$, $O2_b$, $O2_c$, $O3_b$ and $O4_b$ oxygens), interpenetrated by a tetrahedron (made by the $O1_a$, $O2_a$, $O3_a$ and $O4_a$ oxygen atoms, see Fig. 3c), which is along the [001] direction in contact with two subsequent TO_4 tetrahedra, leading to the formation of the

https://doi.org/10.1180/mgm.2024.70 Published online by Cambridge University Press

infinite chain units (Fig. 3a,b). According to the notation used in Fig. 3, the REE-$O2_a$ bond length is significantly longer than the other REE-O bonds, contributing to a significant distortion of the $REEO_9$ polyhedron (Beall et al., 1981; Ni et al., 1995; Clavier et al., 2011), which can be considered as 8+1 coordinated.

Samples and experimental methods

The mineral samples of monazite-(Ce), xenotime-(Y) and chernovite-(Y), investigated in this study, originate from the same locality at Mt. Cervandone (Piedmont, Italian western Alps), where they are found as accessory phases in alpine-type fissures within hydrothermal quartz veins (Graeser and Albertini, 1995) that cross-cut pegmatitic dykes (Guastoni et al., 2006). The latter, intruded in leucocratic gneisses, are enriched in REE and have a strong NYF (Niobium-Yttrium-Fluorine enrichment) signature (Černý, 1991a,b; Černý and Ercit, 2005). An overview of the geological background of the source rocks is described in Pagliaro *et al*. (2022a), along with a detailed chemical analysis of the samples of this study by means of an electron microprobe operating in WDS mode. The measured chemical formulas of the investigated minerals are summarized in Table 1.

In situ high-pressure experiments

In situ high-pressure single-crystal synchrotron X-ray diffraction experiments have been conducted on chernovite-(Y), xenotime-(Y) and monazite-(Ce) at the P02.2 beamline (PETRA-III synchrotron at DESY, Hamburg, Germany) and ID15B beamline (European Synchrotron Radiation Facility, Grenoble, France) using different classes of *P*-transmitting fluids as shown in Table 2. For all the experiments, the crystals were loaded in membrane-driven diamond anvil cells (DAC), equipped with Boehler-Almax designed diamonds/seats. Metallic foils (steel or rhenium) were pre-indented to ca. 40-70 µm and then drilled by spark-erosion to obtain *P*-chambers. Ruby spheres were employed as pressure calibrants (pressure uncertainty ±0.05 GPa; Mao et al., 1986; Chervin et al., 2001). All data collection are based on a ω-rotation with 0.5° per step and 0.5 s (monazite and chernovite) or 1 s (xenotime) of exposure time per frame. At ID15B, X-ray diffraction (XRD) data have been collected using an Eiger2 9M CdTe detector positioned at 179 mm from the sample with a monochromatic 30.2 keV (λ = 0.4099 Å) beam, whereas XRD patterns at P02.2 have been collected on a Perkin Elmer XRD1621 detector at 373 mm from the sample and a monochromatic incident beam with E = 42.67 keV

https://doi.org/10.1180/mgm.2024.70 Published online by Cambridge University Press

(λ = 0.2906 Å). Further details on the beamlines setups are presented in Merlini and Hanfland (2013) and Poreba *et al*. (2022) for ID15B and Rothkirch *et al*. (2013), Liermann *et al*. (2015) and Bykova *et al*. (2019) for P02.2. Indexing of the X-ray diffraction peaks, unit-cell refinements and intensity data reductions were performed using the *CrysAlisPro* package (Rigaku Oxford Diffraction, 2020). Absorption effects, due to the DAC components, were corrected using the semi-empirical ABSPACK routine, implemented in *CrysAlisPro*.

Based on the experimental intensity single-crystal XRD data, the structure refinements were performed using the *Jana2020* software (Petříček et al*.,* 2023), starting from the structural models reported by Pagliaro *et al*. (2022a) for the mineral samples from the same locality. The site occupancy factors of the *A* (lanthanide-bearing) and tetrahedral sites were fixed according to the average chemical composition obtained from EPMA-WDS analysis (Table 1), neglecting the elements with a concentration lower than 0.03 atoms per formula unit and assuming a full occupancy for both the sites. In addition, for monazite-(Ce), the atomic displacement parameters (*ADP*) of the oxygen atoms were refined as isotropic. All the refinements converged with no significant correlations among the refined variables. Refined structural models are deposited as crystallographic information files (cif*s*) in the supplementary materials (online).

For a chernovite-(Y) sample with a slightly larger amount of Ca and Th replacing Y and REE, an *in situ* high-pressure powder XRD experiment has been conducted at the P02.2 beamline of PETRA III (Hamburg, Germany) with a wavelength of λ = 0.2906 Å (42.67 keV) and a Debye-Scherrer geometry. The sample has been loaded into a DAC equipped with Boehler-Almax designed diamonds of 400 µm culet size along with the pressure-transmitting medium (see Table 2 for details) and ruby spheres for pressure determination (*P*-uncertainty ±0.05 GPa; Mao et al., 1986; Chervin et al., 2001). The data collection strategy at any pressure point consisted of a 30° rotation along ω, for an exposure time of 60 s. The X-ray diffraction signals captured by the Perkin Elmer XRD1621 flat panel detector have been finalized and integrated by means of the *Dioptas* software (Prescher and Prakapenka, 2015), in order to remove the background noise due to DAC components and extract the 2ϑ-intensity pattern for any experimental dataset. The unit-cell parameters were determined by fitting the powder XRD data by means of the Rietveld full-profile method using the *GSAS-II* software (Toby and Von Dreele, 2013): the unit-cell parameters, crystallite size, individual scale factor and profile parameters

https://doi.org/10.1180/mgm.2024.70 Published online by Cambridge University Press

(pseudo-Voigt function) have been refined. Moreover, the background signal has been interpolated through a Chebychev polynomial function, with 4 to 15 terms.

In situ high-temperature experiments

In situ high-temperature single-crystal X-ray diffraction data have been collected at the Institute of Mineralogy and Petrography of the University of Innsbruck, using a Stoe IPDS II diffractometer equipped with a Heatstream H*T* device, providing a continuous flow of hot N_2. The primary X-ray beam was generated by an X-ray tube (Mo-anode), operating at 50 kV and 40 mA. A plane graphite monochromator and a multiple pinhole collimator (0.5 mm) were used to guide the beam onto the sample. The image-plate detector was placed at a distance of 100 mm. The temperature calibration had been previously conducted using phase transitions of KNO_3, Ag_2SO_4, K_2SO_4 and K_2CrO_4 powders into glass capillaries. The samples, single crystals of monazite-(Ce), xenotime-(Y) and chernovite-Y (ca. 50-120 μm^3) have been inserted into SiO_2 glass capillaries (0.1 mm in diameter). For all the samples, the data collection consisted in a 180° ω-rotation with a step size of 1° and variable exposure times as reported in Table 2. The temperature accuracy is ≤ 5°C. Further details about the experimental setting are reported in Krüger and Breil (2009). Data collection and reduction has been performed using X-Area (Stoe and Cie, 2008). The indexed cell parameters were always compatible with either the unit cells of chernovite-(Y), xenotime-(Y) or monazite-(Ce).

Structure refinements have been performed based on the single-crystal XRD data adopting the same procedure previously reported for the high-pressure data, and refined structural models are available as *cif* (online supplementary materials). The thermal evolution of significant structural parameters (*i.e.*, *A*-O bonds, *A*-coordination polyhedral and *T*-coordination polyhedral volumes) has been determined from the refined structure models, by means of the tools implemented in the *VESTA3* software (Momma and Izumi, 2011).

In situ high-temperature powder diffraction experiments have been performed on the chernovite sample relatively enriched in Ca and Th at the MCX beamline of the Elettra synchrotron (Basovizza, Trieste Italy), with a wavelength of λ = 0.7293 Å (17 keV) and a Debye-Scherrer setting. The sample, grinded to powder in an agate mortar, has been loaded in a SiO_2 glass capillary (0.3 mm as outer diameter). For any experimental

https://doi.org/10.1180/mgm.2024.70 Published online by Cambridge University Press

point, the data collection strategy consisted in a 2θ-scan between 8° and 60°. A step size of 0.008° has been applied and an equivalent counting time for 1 s/step used. The X-ray diffraction effects have been collected by the high-resolution scintillator detector available at the beamline. During the data collection, the sample was spun at a rate of 1000 rotations per minute along the ϕ-axis. The sample was heated by an air blower, operating between 30 and 1000° C. Further details concerning the experimental setting are reported in Rebuffi *et al*. (2014) and Lausi *et al*. (2015).

Results and discussion

Compressional behaviour of the $REETO_4$ minerals

The evolution of the unit-cell parameters of the investigated samples with pressure is reported in Table S3 and shown in Figs 4 and 5. For monazite-(Ce), the evolution of unit-cell parameters *vs*. *P* shows no evidence of phase transformation in the entire *P*-range investigated. Both the zircon-type minerals, on the other hand, show the occurrence of a phase transition. Chernovite-(Y), at pressures higher than ~10 GPa is no longer stable, undergoing a phase transition to several single-crystal fragments, for which, the position of the peaks in the XRD pattern is compatible with a tetragonal scheelite-type structure. Otherwise, at pressures exceeding ~17 GPa, xenotime-(Y) undergoes a single-crystal to single-crystal phase transition towards a monazite-type structure. For any pressure ramp, the elastic behaviour of the studied mineral has been described by fitting an isothermal Birch-Murnaghan EoS (BM-EoS), truncated at the second or third order, to the *P*-*V* data (a comprehensive description of the BM-EoS formalism can be found in Angel, 2000) using the *EoS-Fit7_GUI* software (Gonzalez-Platas et al., 2016). For monazite, similarly to what observed for the isostructural gasparite-(Ce) by Pagliaro *et al*. (2022b), a change in the compressional behaviour has been detected at ~18 GPa. The parameters refined by fitting the experimental data by BM-EoS are reported in Table 3, among them: the bulk modulus $K_V = \beta_V^{-1} = -V^*(\partial P/\partial V)$ and its pressure derivative $K_V' = (\partial K_V/\partial P)_T$.

The evolution of significant structural parameters (*i.e.*, *A*-O bonds, *A*-coordination polyhedral and *T*-coordination polyhedral volumes) with pressure has been determined, based on the refined structure

https://doi.org/10.1180/mgm.2024.70 Published online by Cambridge University Press

models, by using the *VESTA3* software (Momma and Izumi, 2011). The corresponding values are reported in Table S4.

The results of this study confirm that arsenates are always more compressible than the isostructural phosphates (Table 3), in agreement with the observed relationship that the larger the ionic radii of the *A* and *T* sites, the higher the bulk compressibility (e.g. Zhang et al., 2008; Li et al., 2009; Lacomba-Perales et al., 2010; Errandonea et al., 2011). The refined bulk moduli apparently suggest that monazite-structure type minerals are more compressible than those with a zircon-structure type (Table 3). However, internally consistent theoretical data (Zhang et al., 2008; Li et al., 2009) show that there is a clear increase in compressibility along the lanthanoid series from Lu to La, with a discontinuity in the form of a stiffening when transforming from the zircon to the monazite structure type. Therefore, it can be concluded that, for the investigated minerals, the softening induced by the larger *A* site has a stronger impact than the stiffening induced by the monazite structure type.

The two investigated minerals sharing the zircon structure type, i.e. chernovite-(Y) and xenotime-(Y), undergo different phase transitions paths. Chernovite-(Y) experiences an irreversible transition, from a single-crystal to several crystal fragments, towards a scheelite-type polymorph between ca. 10.5 and 11 GPa. The same phase transition occurs, for synthetic $YAsO_4$ in a powder XRD experiment, in a broader pressure range between 8 and 12 GPa (Errandonea et al., 2011). The apparent discrepancy between these two studies may be ascribed to: *i*) a different kinetics of the phase transition between a single crystal and a polycrystalline material; *ii*) slightly different chemical compositions, as a higher phosphorous content in the presently investigated mineral decreases the average radius of the *T* site; or a combination of both. In general, the same phase transition has already been observed to occur in other ATO_4 compounds, where the pressure of transition increases with the decrease of the *A* and *T* atoms ionic radii (Wang et al., 2004; Zhang et al., 2009; Lacomba-Perales et al., 2010; Errandonea et al., 2011). The relationship between the ionic radii of the *A* and *T* atoms and the type of structure stable at ambient and high-pressure conditions is well known and was first described by Fukunaga and Yamaoka (1979) and Bastide (1987), and later discussed in other publications, e.g. in Lopez-Solano *et al.* (2010). As suggested by the Bastide diagram (Fig. 1) and already reported in the

https://doi.org/10.1180/mgm.2024.70 Published online by Cambridge University Press

literature (Tatsi et al., 2008; Zhang et al., 2009; Lacomba-Perales et al., 2010; Musselman, 2017; Heuser et al., 2018), xenotime-(Y) and isomorphous phosphates undergo a single-crystal to single-crystal phase transition towards a high-pressure polymorph, xenotime-(Y)-II, showing a monazite-type structure. The transition observed in our experiments occurs at a pressure (>17 GPa) consistent with those reported for synthetic YPO_4 compounds (Zhang et al., 2008; Lacomba-Perales et al., 2010). The reversibility of this phase transition is confirmed by this single-crystal study, even though with a significant hysteresis, as the tetragonal polymorph is recovered in decompression only between 6.3 and 1.3 GPa.

Despite a relative scattering between the published values of bulk compressibilities of zircon- and monazite-type phosphates and arsenates, determined on the basis of experimental and theoretical studies, the elastic parameters refined for the mineral species of this study (Table 3) are in agreement with those reported in the literature (Table S1). In the zircon-type minerals chernovite-(Y) and xenotime-(Y), the bulk compression is significantly anisotropic. Indeed, the structure is approximately two times more compressible within the (001) plane than along [001] (Figs 4 and 5, Table S5), which corresponds to the direction of the polyhedral chains evolution. Such a behaviour is strongly controlled by the high tetragonal symmetry, which limits the intra-chain deformation, as confirmed by the behaviour of the two independent *A*-O bond distances, where the *A*-O_a bonds, oriented parallel to [001] (Fig. 2), are the less compressible in both the minerals (Table 4). The bulk compression is therefore mainly accommodated by the AO_8 coordination polyhedron, as suggests its bulk modulus, refined by modelling the polyhedral volume data obtained using *Vesta3* with a II-BM equation of state by means of the *EoS-Fit7-GUI* software (Table 4). For both chernovite-(Y) and xenotime-(Y), bulk moduli values of the *A*-polyhedra are much lower than those obtained for the AsO_4 and PO_4 tetrahedra, which behave as quasi-rigid units (Table 4). The same conclusion can be drawn for monazite-(Ce) (Table 4) and gasparite-(Ce) (Pagliaro et al., 2022b), which, in addition, show that the AsO_4 tetrahedra are slightly more compressible than the PO_4 ones. As previously observed by Pagliaro *et al.* (2022a), the structural features (and responses to external *T* and *P* stimuli) of these compounds are strongly controlled by the crystal chemistry, in particular of the *T* sites. Moreover, not only PO_4 and AsO_4 tetrahedra have a different compressional behaviour, but the nature of the prevailing *T* site controls the size (i.e. the average ionic radius) at ambient conditions of the *A*

https://doi.org/10.1180/mgm.2024.70 Published online by Cambridge University Press

polyhedron (Pagliaro et al., 2022a). This leads, given a similar chemical composition of the *A* site, to slightly larger compressibility's for the more "expanded" *A*-polyhedra of the arsenates among isostructural minerals. The control exerted by the crystal chemistry on the elastic response is also pointed out by the chernovite sample relatively enriched in Ca and Th studied here, which shows a slightly lower bulk modulus value (Table 3). The absence of structure refinements prevents an unambiguous derivation of the structural mechanisms responsible for this behaviour, but it can be suggested that the more "expanded" *A*-polyhedron (due to the higher content of the larger Th and Ca ions, as reported in Table 1) is coherent with the previous observations that a larger average ionic radius of the *A* site generates a softer polyhedron.

The description of the elastic anisotropy in monazite-(Ce) is less straightforward, as the monoclinic symmetry does not allow to rely on the axial compressibilities alone, given the variation of the β angle with pressure. Therefore, the finite Eulerian unit-strain tensor of monazite-(Ce) between ambient-*P* and 18.39 GPa has been calculated using the *Win_Strain* software (Angel, 2011) and with a geometric setting with *X*//*a** and *Y*//*b*. The results show that the principal axes of maximum and minimum unit-strain do not correspond with any of the crystallographic axes, as described by the tensor values in the following matrix:

$$\begin{pmatrix}\varepsilon_1\\ \varepsilon_2\\ \varepsilon_3\end{pmatrix} \measuredangle \begin{pmatrix}158.2(2)^\circ & 90^\circ & 56.2(2)^\circ\\ 90^\circ & 180^\circ & 90^\circ\\ 68.2(2)^\circ & 90^\circ & 33.8(2)^\circ\end{pmatrix} \cdot \begin{pmatrix}a\\ b\\ c\end{pmatrix}$$

The analysis of the finite Eulerian unit-strain tensor allowed the determination of the mean compressibility values along the axes of the strain ellipsoid (with $\varepsilon_1>\varepsilon_2>\varepsilon_3$): ε_1=0.003030(11) GPa^{-1}, ε_2=0.00200(2) GPa^{-1}, ε_3=0.0014(12) GPa^{-1}. The direction of minimum compressibility is within the (010) plane and the anisotropic scheme is ε_1:ε_2:ε_3=2.16:1.43:1. A comparison with the finite Eulerian unit-strain tensor reported for gasparite-(Ce) by Pagliaro *et al*. (2022b) points out that these isostructural minerals share a similar elastic anisotropy. The shared compressional behaviour extends to the structural deformation mechanisms acting on the atomic scale: the nine independent *A*-O bond distances in monazite-(Ce) have different compressional evolutions, as shown in Fig. 7 (see also Table S4). A moderate scattering of the monazite-(Ce) unit-cell parameters can be observed between 10 and 18 GPa, which implied to fit the *V*-*P* data using a Birch-Murnaghan equation of state truncated to the II-order (Table 3). On the basis of the available experimental data and structure

https://doi.org/10.1180/mgm.2024.70 Published online by Cambridge University Press

refinements, it is not possible to unambiguously detect a change in the compressional behaviour at $P < 18$ GPa. On the contrary, a change in the response to compression clearly occurs at pressures exceeding ~ 18.4 GPa, as evidenced by the significant deviation in the high-pressure evolution of the monoclinic β angle (Fig. 5; Table S3), similarly to gasparite-(Ce) (Pagliaro et al. 2022b). This behaviour was already reported for synthetic monazite-type $LaPO_4$ and $CePO_4$ (Huang et al., 2010), but not in another high-pressure investigation of $CePO_4$ (Errandonea et al., 2018). The structure refinements performed in this study allows us to draw a relationship between the change in the elastic behaviour and the structural re-configuration. Fig. 7 and Table S4 show that, at lower pressures, the O_{3c} atom is too far from the *A* site to be considered to effectively belong to its coordination sphere (Fig. 3). However, the *A*-O_{3c} interatomic distance shows a significant shortening under compression (Fig. 7; Table S4), so that, at a pressure consistent with the change in the compressional behaviour, the O_{3c} atom is close enough to the *A* site to enter its coordination sphere, as suggested by the individual bond valences calculated for selected structure refinements and reported in Table S6. As a consequence, the coordination number of the *A* site would increase from 9 (8+1) to 10 (8+2), even though with different contributions from the individual bonds, given the longer bond distances of the of *A*-$O2_a$ and *A*-$O3_c$ (Tables S4 and S6). As the same behaviour was already independently described for gasparite-(Ce) (Pagliaro et al., 2022b) and is analogous to what described to occur at 3.25 GPa in the monazite-type crocoite ($PbCrO_4$, Bandiello et al., 2012; Errandonea and Kumar, 2014), we are inclined to believe that this is an intrinsic feature of the monazite structure type and, therefore, the known transition to a post-baryte-type polymorph at *P* higher than 26 GPa (Ruiz-Fuertes et al., 2016) is accomplished through an intermediate structural configuration, still preserving the monazite symmetry and atomic arrangement, but characterized by an increase from 9 to 10 in the number of the oxygen atoms bonded to the lanthanide-bearing site. This intermediate structural configuration is accomplished, without any clear discontinuity, by a smooth approach of the $O3_c$ atom to the *A* site (where $O3_c$ corresponds to $O3_a$ and $O3_b$ in the coordination sphere of two further *A* atoms). It is worth noting, that the same configuration, with a 10-fold coordinated *A*-site, is also shared by the monazite-type high-pressure polymorph of $CaSO_4$ (Crichton et al., 2005). The higher pressure at which the change of the elastic behaviour occurs in monazite-(Ce) (ca. 18.4 GPa, *vs*. ca. 15 GPa in gasparite-(Ce),

https://doi.org/10.1180/mgm.2024.70 Published online by Cambridge University Press

Pagliaro et al., 2022b) is consistent with the higher *P*-stability expected for the isostructural phosphate with smaller average atomic radii.

Despite affected by larger experimental uncertainties, the same deformation mechanisms described for monazite-(Ce) and gasparite-(Ce) can be derived by the analysis of the refined structural models of the monazite-type high-pressure xenotime-(Y)-II polymorph (Table S4). In this case, the possible occurrence of a change in the compressional behaviour, according to the previous description, should be verified by investigations performed up to higher pressure values, though interatomic *A*-$O3_c$ bond distances around 2.8-2.9 Å (Table S4) can suggest a 10-fold coordinated *A* site. A striking and anomalous feature shown by the experimental results of this study concerns the much larger refined compressibility if compared to what reported in other studies for the same polymorph (K_V = 146(5) GPa in this study; K_V = 206 and 266 GPa in Zhang *et al*. (2009) and Lacomba-Perales *et al*. (2010), respectively). The relatively high number of experimental data of this study leads us to the conclusion that the refined bulk modulus value we obtained is very reliable, implying a similar compressibility between the ambient and high-pressure polymorphs of the investigated xenotime-(Y). It is worth mentioning that a similar compressibility can also be found between the zircon- and monazite-type polymorphs of $LaVO_4$, with K_{V0} = 93(2) GPa (Yuan et al., 2015) and 95(5) GPa (Errandonea et al., 2016), respectively. The thorough re-investigation of the zircon-to-monazite phase transition in xenotime and of the elastic behaviour of the xenotime-II polymorphs appear, therefore, mandatory for a comprehensive understanding.

Thermal behaviour of the $REETO_4$ minerals

The thermal unit-cell parameters evolution from the three *in situ* single-crystal high-*T* ramps on monazite-(Ce), chernovite-(Y) and xenotime-(Y) and from the powder ramp on chernovite-(Y) relatively enriched in Ca and Th are reported in Table S7 and shown in Fig. 6. The thermo-elastic behaviour has been modelled according to the isobaric equation of state modified from Pawley *et al*. (1996) and Holland and Powell (1998) and implemented in the *EoS-Fit7_GUI* (Gonzalez-Platas et al., 2016). The linear thermal expansion coefficients

https://doi.org/10.1180/mgm.2024.70 Published online by Cambridge University Press

have also been refined using the *TEV* software (Langreiter and Kahlenberg, 2015). The refined parameters and the calculated thermal expansion coefficients at ambient conditions $\alpha_V = 1/V^*(\partial V/\partial T)_P$ are reported in Table 3.

A comparison of the linear thermal expansion coefficients refined in this study for xenotime-(Y) and monazite-(Ce) and those already published for the same compounds reveal a good agreement with the literature data (see Table S2 and references therein). However, a significant discrepancy is observed between the values refined for chernovite-(Y) in this study and those previously reported by experimental investigations of $YAsO_4$ (Kahle, 1970; Schopper, 1972; Reddy et al., 1988). As none of the cited references provide experimental unit-cell parameters, nor structure refinements, it is not possible to discuss such a discrepancy, but it is worth noting that the refined values for both the (Ca,Th)-poor and (Ca,Th)-enriched chernovites of this study are self-consistent and diverge from the literature data. With this in mind, future investigation of other natural or synthetic $YAsO_4$-type zircon compounds seems imperative.

A comparative analysis of the thermo-elastic behaviour of the investigated minerals shows that monazite-(Ce) is much more expansible than the two zircon-type compounds (Table 3). In the latter, the [001] direction, i.e the least compressible at high-*P*, is found to be the most expansible at high-*T*. The thermo-elastic anisotropy of monazite-(Ce) cannot be directly described based on the unit-cell parameters behaviour, given its monoclinic symmetry. The thermal expansion of monazite-(Ce) has been modelled with the *TEV* software (Langreiter and Kahlenberg,, 2015) and at the temperature of 400 °C (i.e. ΔT ~ 380 °C) its relationship with the unit-cell axes is described by the following matrix:

$$\begin{pmatrix}\alpha_1\\ \alpha_2\\ \alpha_3\end{pmatrix} \angle \begin{pmatrix}109.02° & 90° & 5.47°\\ 19.02° & 90° & 84.531°\\ 90° & 0° & 90°\end{pmatrix} \cdot \begin{pmatrix}a\\ b\\ c\end{pmatrix}$$

The mean thermal expansivity along the axes of the unit-strain ellipsoid, determined at 400°C, is: α_1 = $11.56\cdot10^{-6}$ K^{-1}, α_2 = $9.93\cdot10^{-6}$ K^{-1} and α_3 = $7.39\cdot10^{-6}$ K^{-1}, leading to the anisotropic scheme α_1: α_2: α_3 = 1.56:1.34:1.

https://doi.org/10.1180/mgm.2024.70 Published online by Cambridge University Press

The structure refinements (thermal evolution of selected structural parameters is reported in Table S8) showed that for the zircon-type minerals xenotime-(Y) and chernovite-(Y), the coordination polyhedron hosting the lanthanides ions (*A*-polyhedron) has a paramount role in accommodating the bulk thermal expansion, being its refined thermal expansivity almost the double of the value referred to the unit-cell volume (Tables 3, 4), whereas the two independent *A*-O bond distances show a comparable behaviour, differently from what shown at high-*P* (Table S8). In monazite-(Ce) as well, the *A*-polyhedron plays a significant role in accommodating the thermal expansion, but of a lesser magnitude with respect to the tetragonal minerals (Tables 3, 4), given the larger degrees of freedom for structure deformation induced by the monoclinic symmetry. In all the cases, it is worth noting that the tetrahedra, being them PO_4 or AsO_4, appear to behave as rigid units in the temperature range investigated (Table 4).

As a general observation based on the experimental data of this study, xenotime-(Y) appears more expansible with temperature than chernovite-(Y). Even though the discrepancy between our data and the previously published thermal expansion behaviour of other $YAsO_4$ compounds (Kahle, 1970; Schopper, 1972; Reddy et al., 1988) suggests caution in this regards. However, our observation is consistent with the results reported by Li et al. (2009) for APO_4 and $AAsO_4$ (A = lanthanides) and based on theoretical calculations of lattice energies, where phosphates always show a larger expansibility than isostructural arsenates sharing the same A cation for both the zircon and monazite structural types.

Concluding remarks

The experimental data reported in this study, along with those published by Pagliaro *et al.* (2022b) on the high-pressure behaviour of gasparite-(Ce), provide a suite of thermo-elastic parameters for natural lanthanides-bearing phosphates and arsenates outcropping in the hydrothermal veins of the Mt. Cervandone.

Consistently with the previous scientific literature, the two zircon-type minerals undergo different *P*-induced phase transitions. Chernovite-(Y) above ~10 GPa converts to a scheelite-type polymorph, whereas xenotime-

https://doi.org/10.1180/mgm.2024.70 Published online by Cambridge University Press

(Y) above ~ 17 GPa transforms into a monazite-type polymorph by a reconstructive phase transition single-crystal to single-crystal in character.

The monazite-type phosphates and arsenates do not undergo any phase transitions in the explored pressure range of this study. However, the analysis of the compressional evolution of the unit-cell parameters and of the crystal structures of monazite-(Ce) (this study) and gasparite-(Ce) from the same locality (Pagliaro et al., 2022b), highlighted a change in the compressional behaviour occurring at ~ 18 and 15 GPa, respectively. This is related, for both the minerals, to a structural re-arrangement involving the smooth approach of a tenth oxygen atom into the coordination sphere of the lanthanide-bearing *A* site, which increases its coordination from 9 (8+1) to 10 (8+2) before the expected phase transition to a high-pressure polymorph. A general conclusion from both the present experiments and previous studies is that, despite the numerous papers publishing high-quality data on these crystalline compounds relevant to Earth and Materials sciences, there are still unexplored regions, whose physical-chemical features should be described by the adoption of up-to-date experimental techniques, facilities and crystallographic methods.

The analysis of the elastic and structural response with pressure and temperature of the investigated minerals of this study, and of gasparite-(Ce) (Pagliaro et al., 2022b), let us conclude that their compressional and thermal behaviours are not, as commonly observed, induced by the same mechanisms opposite in sign. For example, phosphates are less compressible than the isostructural arsenates, but at high temperature they are *more* expansible. In the same way, the zircon-type structure is less compressible along the **c** crystallographic direction, but at high-*T* along the same direction the higher expansivity is shown. This behaviour can be explained by the significant control exerted on these compounds by the chemical strain. As described by Pagliaro *et al*. (2022a), the chemical nature of the *T* cations (P or As) has a paramount role in controlling not only the TO_4 tetrahedra, but also the other structural parameters: the substitution of P by As not only expands the tetrahedron, but the *A* coordination polyhedron too (at the same chemical composition of the *A* site). This study shows that the chemically more "expanded" structures of the arsenates are more compressible than the chemically more "compressed" structures of phosphates, but in response to a thermal

https://doi.org/10.1180/mgm.2024.70 Published online by Cambridge University Press

perturbation they show the opposite behaviour being less expansible. Such an observation is confirmed by the slightly different behaviours of the two investigated chernovite samples. The sample relatively enriched in Th and Ca, due to the larger ionic radii of these cations with respect to the dominant Y in the *A* site, show a chemical expansion at ambient conditions (as described in Pagliaro et al., 2022a) that is reflected by a slightly larger compressibility at high pressure and a slightly lower expansivity at high temperature.

Acknowledgements

This manuscript is dedicated to the memory of our friend and colleague Dr. Alessandro Guastoni (1966-2022), who has given a significant contribution in the conceptualization of this study. FP, GDG and PL are grateful to Alessandro for the numerous and fruitful discussions on this and many other topics.

The editors and two anonymous reviewers are acknowledged for the handling of the manuscript and for the fruitful and insightful comments. We acknowledge DESY (Hamburg, Germany), a member of the Helmholtz Association HGF, for the provision of experimental facilities. Parts of this research were carried out at PETRA III. Beamtime was allocated for proposals I-20210452 EC and I-20211179 EC. We acknowledge Elettra Sincrotrone Trieste for providing access to its synchrotron radiation facilities. We acknowledge the European Synchrotron Radiation Facility (ESRF) for provision of synchrotron radiation facilities. The research leading to this result has been supported by the project CALIPSOplus under Grant Agreement 730872 from the EU Framework Programme for Research and Innovation HORIZON 2020. FP, DC, TB, GDG and PL acknowledge the Italian Ministry of University for the support through the project "Dipartimenti di Eccellenza 2023-2027". DC, GDG and PL acknowledge the University of Milan for the support through the project "Piano di sostegno alla Ricerca 2022".

Competing interests

The authors declare none.

https://doi.org/10.1180/mgm.2024.70 Published online by Cambridge University Press

References

Angel R.J. (2000) Equations of State. *Reviews in Mineralogy and Geochemistry*, **41**, 35–59. https://doi.org/10.2138/rmg.2000.41.2

Angel R.J. (2011) *Win_Strain: A program to calculate strain tensors from unit-cell parameters*. http://www.rossangel.com/home.htm

Angel R.J., Bujak M., Zhao J., Gatta G.D. and Jacobsen S.D. (2007) Effective hydrostatic limits of pressure media for high-pressure crystallographic studies. *Journal of Applied Crystallograhy*, **40**, 26-32. DOI: 10.1107/S0021889806045523.

Bandiello E., Errandonea D., Martinez-Garcia D., Santamaria-Perez D. and Manjón F.J. (2012) Effects of high-pressure on the structural, vibrational, and electronic properties of monazite-type $PbCrO_4$. *Physical Review B*, **85**, 024108. DOI: 10.1103/PhysRevB.85.024108.

Bastide J.P. (1987) Systématique simplifiée des composés ABX_4 ($X = O^{2-}$, F^-) et evolution possible de leurs structures cristallines sous pression. *Journal of Solid State Chemistry*, **71**, 115–120. https://doi.org/10.1016/0022-4596(87)90149-6

Beall G.W., Boatner L.A., Mullica D.F. and Milligan W.O. (1981) The structure of cerium orthophosphate, a synthetic analogue of monazite. *Journal of Inorganic and Nuclear Chemistry*, **43**, 101–105. https://doi.org/10.1016/0022-1902(81)80443-5

Binks W. (1926) The crystalline structure of zircon. *Mineralogical Magazine and Journal of the Mineralogical Society*, **21**, 176–187. https://doi.org/10.1180/minmag.1926.021.115.06

Boatner L.A. (2002) Synthesis, Structure, and Properties of Monazite, Pretulite, and Xenotime. *Reviews in Mineralogy and Geochemistry*, **48**, 87–121. https://doi.org/10.2138/rmg.2002.48.4

Bragg W.L. (1929) Atomic arrangement in the silicates. *Transactions of the Faraday Society*, **25**, 291. https://doi.org/10.1039/TF9292500291

https://doi.org/10.1180/mgm.2024.70 Published online by Cambridge University Press

Brown I.D. (2002) *The chemical bond in inorganic chemistry : the bond valence model*. Oxford University Press, Oxford, 288 pp.

Bykova E., Aprilis G., Bykov M., Glazyrin K., Wendt M., Wenz S., Liermann H-P., Roeh J.T., Ehnes A., Dubrovinskaia N. and Dubrovinsky L. (2019) Single-crystal diffractometer coupled with double-sided laser heating system at the Extreme Conditions Beamline P02.2 at PETRAIII. *Review of Scientific Instruments*, **90**, 73907. https://doi.org/10.1063/1.5108881

Cerny P. and Ercit T.S. (2005) The classification of granitic pegmatites revisited. *The Canadian Mineralogist*, **43**, 2005–2026. https://doi.org/10.2113/gscanmin.43.6.2005

Černý P. (1991a) Rare-element granitic pegmatites. Part I: Anatomy and internal evolution of pegmatite deposits. *Geoscience Canada*, **18**, 49–67

Černý P. (1991b) Rare-element granitic pegmatites. Part II: Regional to global environments and petrogenesis. *Geoscience Canada*, **18**, 68–81

Chervin J.C., Canny B. and Mancinelli M. (2001) Ruby-spheres as pressure gauge for optically transparent high pressure cells. *High Pressure Research*, **21**, 305–314. https://doi.org/10.1080/08957950108202589

Clavier N., Podor R. and Dacheux N. (2011) Crystal chemistry of the monazite structure. *Journal of the European Ceramic Society*, **31**, 941–976. https://doi.org/10.1016/j.jeurceramsoc.2010.12.019

Crichton W.A., Parise J.B., Antao S.M. and Grzechnik A. (2002) Evidence for monazite-, barite-, and $AgMnO_4$ (distorted barite)-type structures of $CaSO_4$ at high pressure and temperature. *American Mineralogist*, **90**, 22-27. DOI: 10.2138/am.2005.1654.

Crichton W.A., Merlini M., Müller H., Chantel J. and Hanfland M. (2012) The high-pressure monazite-to-scheelite transformation in $CaSeO_4$. *Mineralogical Magazine*, **76**, 913–923. https://doi.org/10.1180/minmag.2012.076.4.08

https://doi.org/10.1180/mgm.2024.70 Published online by Cambridge University Press

Davis J.B., Marshall D.B., Housley R.M. and Morgan P.E.D. (1998) Machinable Ceramics Containing Rare-Earth Phosphates. *Journal of the American Ceramic Society*, **81**, 2169–2175. https://doi.org/10.1111/j.1151-2916.1998.tb02602.x

Errandonea D. (2017) High-pressure phase transitions and properties of MTO_4 compounds with the monazite-type structure. *Physica Status Solidi B*, **254**, 1700016. https://doi.org/10.1002/pssb.201700016

Errandonea D. and Kumar R.S. (2014) High-pressure structural transformations of $PbCrO_4$ up to 51.2 GPa: An angle-dispersive synchrotron X-ray diffraction study. *Materials Research Bulletin*, **60**, 206-211. DOI: https://doi.org/10.1016/j.materresbull.2014.08.041.

Errandonea D., Lacomba-Perales R., Ruiz-Fuertes J., Segura A., Achary S.N. and Tyagi A.K. (2009) High-pressure structural investigation of several zircon-type orthovanadates. *Physical Review B*, **79**, 184104. https://doi.org/10.1103/PhysRevB.79.184104.

Errandonea D., Kumar R., López-Solano J., Rodríguez-Hernández P., Muñoz A., Rabie M.G. and Sáez Puche R. (2011) Experimental and theoretical study of structural properties and phase transitions in $YAsO_4$ and $YCrO_4$. *Physical Review B*, **83**, 245. https://doi.org/10.1103/PhysRevB.83.134109

Errandonea D., Pellicer-Porres J., Martínez-García D., Ruiz-Fuertes J., Friedrich A., Morgenroth W., Popescu C., Rodríguez-Hernández P., Muñoz A. and Bettinelli M. (2016) Phase Stability of Lanthanum Orthovanadate at High Pressure. *Journal of Physical Chemistry C*, **120**, 13749–13762. https://doi.org/10.1021/acs.jpcc.6b04782

Errandonea D., Gomis O., Rodríguez-Hernández P., Muñoz A., Ruiz-Fuertes J., Gupta M., Achary S.N., Hirsch A., Manjon F.J., Peters L., Roth G., Tyagi A.K. and Bettinelli M. (2018) High-pressure structural and vibrational properties of monazite-type $BiPO_4$, $LaPO_4$, $CePO_4$, and $PrPO_4$. *Journal of Physics: Condensed Matter*, **30**, 65401. https://doi.org/10.1088/1361-648X/aaa20d

Finch R.J. and Hanchar J.M.(2003) Structure and Chemistry of Zircon and Zircon-Group Minerals. *Reviews in Mineralogy and Geochemistry*, **53**, 1–25. https://doi.org/10.2113/0530001

https://doi.org/10.1180/mgm.2024.70 Published online by Cambridge University Press

Fukunaga O. and Yamaoka S. (1979) Phase transformations in ABO_4 type compounds under high pressure. *Physics and Chemistry of Minerals*, **5**, 167–177. https://doi.org/10.1007/BF00307551

Gleissner J., Errandonea D., Segura A., Pellicer-Porres J., Hakeem M.A., Proctor J.E., Raju S.V., Kumar R.S., Rodríguez-Hernández P., Muñoz A., Lopez-Moreno S. and Bettinelli M. (2016) Monazite-type $SrCrO_4$ under compression. *Physical Review B*, **94**, 134108. https://doi.org/10.1103/PhysRevB.94.134108

Gonzalez-Platas J., Alvaro M., Nestola F. and Angel R.J. (2016) EosFit7-GUI: a new graphical user interface for equation of state calculations, analyses and teaching. *Journal of Applied Crystallography*, **49**, 1377–1382. https://doi.org/10.1107/S1600576716008050

Graeser S. and Albertini C. (1995) Wannigletscher und Conca Cervandone. *Lapis*, **20**, 41-64.

Guastoni A., Pezzotta F. and Vignola P. (2006) Characterization and genetic inferences of arsenates, sulfates and vanadates of Fe, Cu, Pb, Zn from Mount Cervandone (Western Alps, Italy). *Periodico di Mineralogia*, **75**, 141–150

Harrison T.M., Catlos E.J. and Montel J-M. (2002) U-Th-Pb Dating of Phosphate Minerals. *Reviews in Mineralogy and Geochemistry*, **48**, 524–558. https://doi.org/10.2138/rmg.2002.48.14

Hassel O. (1926) XIV. Die Kristallstruktur einiger Verbindungen von der Zusammensetzung MRO_4. I. Zirkon $ZrSiO_4$. *Zeitschrift für Kristallographie - Crystalline Materials*, **63**, 247–254. https://doi.org/10.1524/zkri.1926.63.1.247

Hay R.S., Mogilevsky P. and Boakye E. (2013) Phase transformations in xenotime rare-earth orthophosphates. *Acta Materialia*, **61**, 6933–6947. https://doi.org/10.1016/j.actamat.2013.08.005

Heuser J.M., Palomares R.I., Bauer J.D., Rodriguez M.L., Cooper J., Lang M., Scheinost A.C., Schlenz H., Winkler B., Bosbach D., Neumeier S. and Deissmann G. (2018) Structural characterization of $(Sm,Tb)PO_4$ solid solutions and pressure-induced phase transitions. *Journal of the European Ceramic Society*, **38**, 4070–4081. https://doi.org/10.1016/j.jeurceramsoc.2018.04.030

https://doi.org/10.1180/mgm.2024.70 Published online by Cambridge University Press

Holland T.J.B. and Powell R. (1998) An internally consistent thermodynamic data set for phases of petrological interest. *Journal Metamorphic Geology*, **16**, 309–343. https://doi.org/10.1111/j.1525-1314.1998.00140.x

Huang T., Lee J-S., Kung J. and Lin C-M. (2010) Study of monazite under high pressure. *Solid State Communications*, **150**, 1845–1850. https://doi.org/10.1016/j.ssc.2010.06.042

Jayaraman A., Kourouklis G.A., Espinosa G.P., Cooper A.S. and van Uitert L.G. (1987) A high-pressure Raman study of yttrium vanadate (YVO_4) and the pressure-induced transition from the zircon-type to the scheelite-type structure. *Journal of Physics and Chemistry of Solids*, **48**, 755–759. https://doi.org/10.1016/0022-3697(87)90072-2

Kahle H.G., Schopper H.C., Urban W. and Wüchner W. (1970) Temperature Effects on Zircon Structure Lattice Parameters and Zero-Field Resonance for Substituted Gd^{3+}. *Physica Status Solidi B*, **38**, 815–819. https://doi.org/10.1002/pssb.19700380231

Klotz S., Chervin J-C., Munsch P. and Le Marchand G. (2009) Hydrostatic limits of 11 pressure transmitting media. *Journal of Physics D*, **42**, 075413. http://dx.doi.org/10.1088/0022-3727/42/7/075413.

Kolitsch U. and Holtstam D. (2004) Crystal chemistry of $REEXO_4$ compounds (X = P,As,V). II. Review of $REEXO_4$ compounds and their stability fields. *European Journal of Mineralogy*, **16**, 117–126. https://doi.org/10.1127/0935-1221/2004/0016-0117

Kolitsch U., Holtstam D. and Gatedal K. (2004) Crystal chemistry of $REEXO_4$ compounds (X = P,As,V). I. Paragenesis and crystal structure of phosphatian gasparite-(Ce) from the Kesebol Mn-Fe-Cu deposit, Vastra Gotaland, Sweden. *European Journal of Mineralogy*, **16**, 111–116. https://doi.org/10.1127/0935-1221/2004/0016-0111

Krüger H. and Breil L. (2009) Computer-controlled high-temperature single-crystal X-ray diffraction experiments and temperature calibration. *Journal of Applied Crystallography*, **42**, 140–142. https://doi.org/10.1107/S0021889808035607

https://doi.org/10.1180/mgm.2024.70 Published online by Cambridge University Press

Lacomba-Perales R., Errandonea D., Meng Y. and Bettinelli M. (2010) High-pressure stability and compressibility of APO_4 (A=La , Nd, Eu, Gd, Er, and Y) orthophosphates: An x-ray diffraction study using synchrotron radiation. *Physical Review B*, **81**, 21. https://doi.org/10.1103/PhysRevB.81.064113

Langreiter T. and Kahlenberg V. (2015) TEV—A Program for the Determination of the Thermal Expansion Tensor from Diffraction Data. *Crystals*, **5**, 143–153. https://doi.org/10.3390/cryst5010143

Lausi A., Polentarutti M., Onesti S., Plaisier J.R., Busetto E., Bais G., Barba L., Cassetta A., Campi G., Lamba D., Pifferi A., Mande S.C., Sarma D.D., Sharma S.M. and Paolucci G. (2015) Status of the crystallography beamlines at Elettra. *European Physical Journal Plus*, **130**, 2476. https://doi.org/10.1140/epjp/i2015-15043-3

Li H., Zhang S., Zhou S. and Cao X. (2009) Bonding characteristics, thermal expansibility, and compressibility of RXO(4) (R = rare earths, X = P, As) within monazite and zircon structures. *Inorganic Chemistry*, **48**, 4542–4548. https://doi.org/10.1021/ic900337j

Liermann H-P. et al. (2015) The Extreme Conditions Beamline P02.2 and the Extreme Conditions Science Infrastructure at PETRA III. *Journal of Synchrotron Radiation*, **22**, 908-24. https://doi.org/10.1107/s1600577515005937.

López-Solano J, Rodríguez-Hernández P, Muñoz A, Gomis O, Santamaría-Perez D, Errandonea D, Manjón FJ, Kumar RS, Stavrou E, Raptis C (2010) Theoretical and experimental study of the structural stability of TbPO4 at high pressures. Phys. Rev. B 81:21. https://doi.org/10.1103/PhysRevB.81.144126

Manjón FJ, Rodríguez-Hernández P, Muñoz A, Romero AH, Errandonea D, Syassen K (2010) Lattice dynamics of YVO4 at high pressures. Phys. Rev. B 81:90. https://doi.org/10.1103/PhysRevB.81.075202

Mao HK, Xu J, Bell PM (1986) Calibration of the ruby pressure gauge to 800 kbar under quasi-hydrostatic conditions. J. Geophys. Res. 91:4673–4676. https://doi.org/10.1029/JB091iB05p04673

Marqueño T, Errandonea D, Pellicer-Porres J, Santamaria-Perez D, Martinez-Garcia D, Bandiello E, Rodriguez-Hernandez P, Muñoz A, Achary SN, Popescu C (2021) Polymorphism of praseodymium orthovanadate under high pressure. Phys. Rev. B 103. https://doi.org/10.1103/PhysRevB.103.134113

https://doi.org/10.1180/mgm.2024.70 Published online by Cambridge University Press

Merlini M, Hanfland M (2013) Single-crystal diffraction at megabar conditions by synchrotron radiation. High Pressure Research 33:511–522. https://doi.org/10.1080/08957959.2013.831088

Momma K, Izumi F (2011) VESTA 3 for three-dimensional visualization of crystal, volumetric and morphology data. J Appl Crystallogr 44:1272–1276. https://doi.org/10.1107/S0021889811038970

Mooney RCL (1948) Crystal Structures of a Series of Rare Earth Phosphates. The Journal of Chemical Physics 16:1003. https://doi.org/10.1063/1.1746668

Morgan PED, Marshall DB, Housley RM (1995) High-temperature stability of monazite-alumina composites. Materials Science and Engineering: A 195:215–222. https://doi.org/10.1016/0921-5093(94)06521-7

Mullica DF, Milligan WO, Grossie DA, Beall GW, Boatner LA (1984) Ninefold coordination LaPO4: Pentagonal interpenetrating tetrahedral polyhedron. Inorganica Chimica Acta 95:231–236. https://doi.org/10.1016/S0020-1693(00)87472-1

Musselman MA (2017) In situ Raman spectroscopy of pressure-induced phase transformations in DyPO4 and GdxDy(1-x)PO4, Colorado School of Mines

Ni Y, Hughes JM, Mariano AN (1995) Crystal chemistry of the monazite and xenotime structures. American Mineralogist 80:21–26. https://doi.org/10.2138/am-1995-1-203

Oelkers EH, Montel J-M (2008) Phosphates and Nuclear Waste Storage. Elements 4:113–116. https://doi.org/10.2113/GSELEMENTS.4.2.113

Orlova AI, Ojovan MI (2019) Ceramic Mineral Waste-Forms for Nuclear Waste Immobilization. Materials (Basel) 12. https://doi.org/10.3390/ma12162638

Pagliaro F, Lotti P, Comboni D, Battiston T, Guastoni A, Fumagalli P, Rotiroti N, Gatta GD (2022 a) High-pressure behaviour of gasparite-(Ce) (nominally CeAsO4), a monazite-type arsenate. Phys Chem Minerals 49:569. https://doi.org/10.1007/s00269-022-01222-5

https://doi.org/10.1180/mgm.2024.70 Published online by Cambridge University Press

Pagliaro F, Lotti P, Guastoni A, Rotiroti N, Battiston T, Gatta GD (2022b) Crystal chemistry and miscibility of chernovite-(Y), xenotime-(Y), gasparite-(Ce) and monazite-(Ce) from Mt. Cervandone, Western Alps, Italy. Mineral. Mag. 86:150–167. https://doi.org/10.1180/mgm.2022.5

Panchal V, Errandonea D, Manjón FJ, Muñoz A, Rodríguez-Hernández P, Achary SN, Tyagi AK (2017) High-pressure lattice-dynamics of $NdVO_4$. Journal of Physics and Chemistry of Solids 100:126–133. https://doi.org/10.1016/j.jpcs.2016.10.001

Parrish W (1939) Unit cell and space group of monazite,$(La,Ce,Y)PO_4$. American Mineralogist:651–652

Pawley AR, Redfern SAT, Holland TJB (1996) Volume behaviour of hydrous minerals at high pressure and temperature; I, Thermal expansion of lawsonite, zoisite, clinozoisite, and diaspore. American Mineralogist 81:335–340. https://doi.org/10.2138/am-1996-3-407

Perrière L, Bregiroux D, Naitali B, Audubert F, Champion E, Smith DS, Bernache-Assollant D (2007) Microstructural dependence of the thermal and mechanical properties of monazite LnPO4 (Ln=La to Gd). Journal of the European Ceramic Society 27:3207–3213. https://doi.org/10.1016/j.jeurceramsoc.2006.12.005

Petříček V, Palatinus L, Plàšil J, Dušek M, (2023) JANA2020 – a new version of the crystallographic computing system JANA. Zeitschrift für Kristallographie - Crystalline Materials 238:271–282. https://doi.org/10.1515/zkri-2023-0005

Poreba T, Comboni D, Mezouar M, et al (2022) Tracking of Structural Phase Transitions via Single Crystal X-ray Diffraction at Extreme Conditions: Advantages of Extremely Brilliant Source. J. Phys. Condens. Matter 35. https://doi.org/10.1088/1361-648X/aca50b

Prescher C, Prakapenka VB (2015) DIOPTAS : a program for reduction of two-dimensional X-ray diffraction data and data exploration. High Pressure Research 35:223–230. https://doi.org/10.1080/08957959.2015.1059835

https://doi.org/10.1180/mgm.2024.70 Published online by Cambridge University Press

Rapp RP, Watson EB (1986) Monazite solubility and dissolution kinetics: implications for the thorium and light rare earth chemistry of felsic magmas. Contr. Mineral. and Petrol. 94:304–316. https://doi.org/10.1007/BF00371439

Rebuffi L, Plaisier JR, Abdellatief M, Lausi A, Scardi P (2014) MCX: a Synchrotron Radiation Beamline for X-ray Diffraction Line Profile Analysis. Zeitschrift anorg allge chemie 640:3100–3106. https://doi.org/10.1002/zaac.201400163

Reddy CVV, Satyanarayana Murthy K, Kistaiah P (1988) X-ray study of the thermal expansion anisotropy in YVO_4 and $YAsO_4$ compounds. Solid State Communications 67:545–547. https://doi.org/10.1016/0038-1098(84)90179-0

Rigaku Oxford Diffraction (2020) CrysAlisPro version 171.41.93, Wroclaw, Poland

Rothkirch A, Gatta GD, Meyer M, Merkel S, Merlini M, Liermann HP (2013) Single-crystal diffraction at the Extreme Conditions beamline P02.2: procedure for collecting and analyzing high-pressure single-crystal data. J Synchrotron Radiat 20:711–720. https://doi.org/10.1107/S0909049513018621

Ruiz-Fuertes J, Hirsch A, Friedrich A, Winkler B, Bayarjargal L, Morgenroth W, Peters L, Roth G, Milman V (2016) High-pressure phase of LaPO4 studied by x-ray diffraction and second harmonic generation. Phys. Rev. B 94:203. https://doi.org/10.1103/PhysRevB.94.134109

Schopper HC, Urban W, Ebel H (1972) Measurements of the temperature dependence of the lattice parameters of some rare earth compounds with zircon structure. Solid State Communications 11:955–958. https://doi.org/10.1016/0038-1098(72)90297-9

Sousa Filho PC de, Serra OA (2009) Red, green, and blue lanthanum phosphate phosphors obtained via surfactant-controlled hydrothermal synthesis. Journal of Luminescence 129:1664–1668. https://doi.org/10.1016/j.jlumin.2009.04.075

Stagarone C, Angel RJ, Prencipe M, Mihailova B, Alvaro M (2019) New insights into the zircon-reidite phase transition. American Mineralogist 104:830-837.

https://doi.org/10.1180/mgm.2024.70 Published online by Cambridge University Press

Stoe & Cie (2008) WinXpose 1.7.6, Darmstadt, Germany

Strada M, Schwendimann G (1934) La struttura cristallina di alcuni fosfati ed arseniati di metalli trivalenti. II. Arseniato e fosfato di yttrio. Gazzetta Chimica Italiana:662–674

Strzelecki AC, Zhao X, Estevenon P, Xu H, Dacheux N, Ewing RC, Guo X (2024) Crystal chemistry and thermodynamic properties of zircon structure-type materials. American Mineralogist 109:225–242. https://doi.org/10.2138/am-2022-8632

Subbarao EC, Agrawal DK, McKinstry HA, Sallese CW, Roy R (1990) Thermal Expansion of Compounds of Zircon Structure. Journal of the American Ceramic Society 73:1246–1252. https://doi.org/10.1111/j.1151-2916.1990.tb05187.x

Tatsi A, Stavrou E, Boulmetis YC, Kontos AG, Raptis YS, Raptis C (2008) Raman study of tetragonal $TbPO_4$ and observation of a first-order phase transition at high pressure. J. Phys.: Condens. Matter 20:425216. https://doi.org/10.1088/0953-8984/20/42/425216

Toby BH, Dreele RB von (2013) GSAS-II : the genesis of a modern open-source all purpose crystallography software package. J Appl Crystallogr 46:544–549. https://doi.org/10.1107/S0021889813003531

Ueda T (1953) The Crystal Structure of Monazite ($CePO_4$). Memoirs of the College of Science, University of Kyoto, Series B:227–246

UEDA T (1967) Reexamination of the crystal structure of monazite. J. Japan. Assoc. Min. Petr. Econ. Geol. 58:170–179. https://doi.org/10.2465/ganko1941.58.170

Ushakov SV, Helean KB, Navrotsky A, Boatner LA (2001) Thermochemistry of rare-earth orthophosphates. J. Mater. Res. 16:2623–2633. https://doi.org/10.1557/JMR.2001.0361

Vegard L (1916) VI. Results of crystal analysis. The London, Edinburgh, and Dublin Philosophical Magazine and Journal of Science 32:65–96. https://doi.org/10.1080/14786441608635544

https://doi.org/10.1180/mgm.2024.70 Published online by Cambridge University Press

Vegard L (1926) CIV. Results of crystal analysis. The London, Edinburgh, and Dublin Philosophical Magazine and Journal of Science 1:1151–1193. https://doi.org/10.1080/14786442608633716

Vegard L (1927) XLVII. The structure of xenotime and the relation between chemical constitution and crystal structure. The London, Edinburgh, and Dublin Philosophical Magazine and Journal of Science 4:511–525. https://doi.org/10.1080/14786440908564357

Vorres KS (1962) Correlating ABO_4 compound structures. J. Chem. Educ. 39:566. https://doi.org/10.1021/ed039p566

Wang B (2023) Pressure-induced structural phase transitions in natural monazite. Phys. Rev. B 107. https://doi.org/10.1103/PhysRevB.107.104102

Wang X, Loa I, Syassen K, Hanfland M, Ferrand B (2004) Structural properties of the zircon- and scheelite-type phases of YVO_4 at high pressure. Phys. Rev. B 70:449. https://doi.org/10.1103/PhysRevB.70.064109

Wyckoff RWG, Hendricks SB (1928) IV. Die Kristallstruktur von Zirkon und die Kriterien für spezielle Lagen in tetragonalen Raumgruppen. Zeitschrift für Kristallographie - Crystalline Materials 66:73–102. https://doi.org/10.1524/zkri.1928.66.1.73

Yuan H, Wang K, Wang C, Zhou B, Yang K, Liu J, Zou B (2015) Pressure-Induced Phase Transformations of Zircon-Type $LaVO_4$ Nanorods. J. Phys. Chem. C 119:8364–8372. https://doi.org/10.1021/acs.jpcc.5b01007

Zhang S, Zhou S, Li H, Li L (2008) Investigation of thermal expansion and compressibility of rare-earth orthovanadates using a dielectric chemical bond method. Inorg Chem 47:7863–7867. https://doi.org/10.1021/ic800672h

https://doi.org/10.1180/mgm.2024.70 Published online by Cambridge University Press

Fig. 1. The so-called Bastide diagram shows the relationships among structural types as a function of the atomic radii of cations at the *A* site (r_A), *T* site (r_T) and oxygen (r_O), within the ATO_4 family. The fields corresponding to the $SrUO_4$ and $BaWO_4$-II structures are labelled as orthorhombic (*Cmca*, *Pbcm*, *Pnma*) and monoclinic 14, respectively (2, 10, 12, 14 refer to the space group numbers). The post-baryte field is not reported (modified after López-Solano et al., 2010).

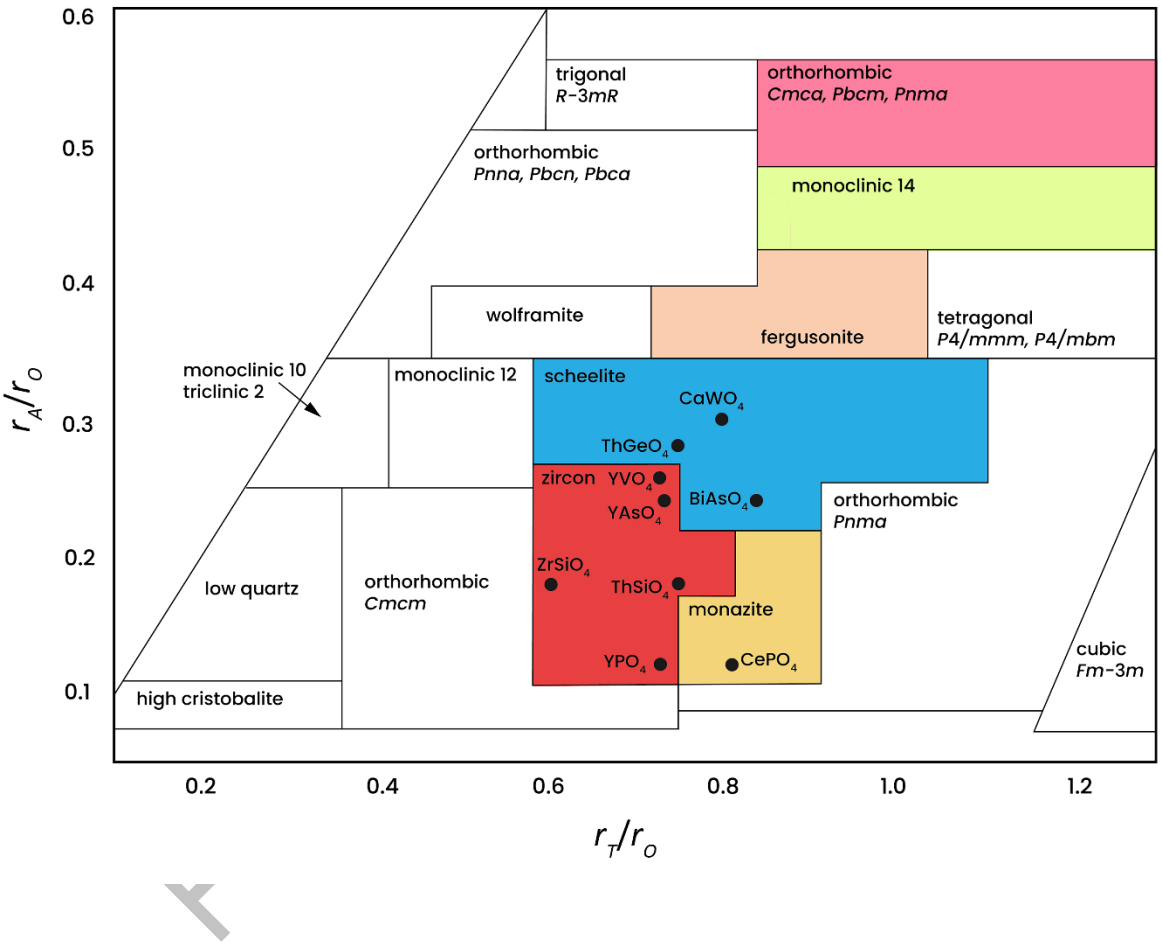

https://doi.org/10.1180/mgm.2024.70 Published online by Cambridge University Press

Fig. 2. Crystal structure of the zircon-type materials viewed (a) along the [010] and (b) [001] directions and showing (c) the chains running along the **c** directions and the bond distances configuration among the AO_8 polyhedron, and (d) a side view of the overall crystal structure.

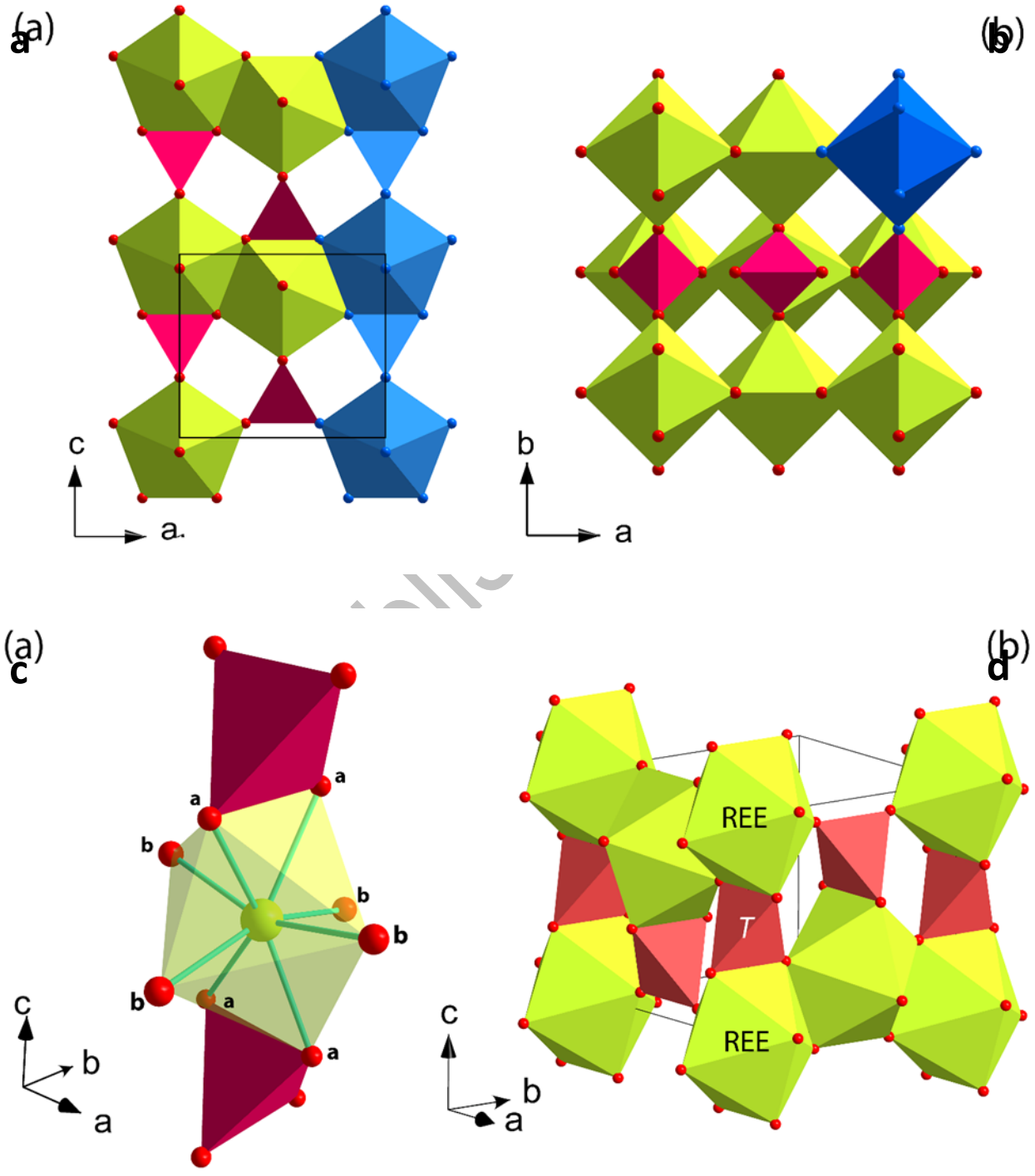

https://doi.org/10.1180/mgm.2024.70 Published online by Cambridge University Press

Fig. 3. Crystal structure of monazite, viewed along (a) the [100] and (b) [010] directions; a chain-like unit is highlighted in blue; (c) coordination polyhedron of the REE-bearing *A* site, with 9 independent *A*-O bonds; (d) general view of the monazite structure.

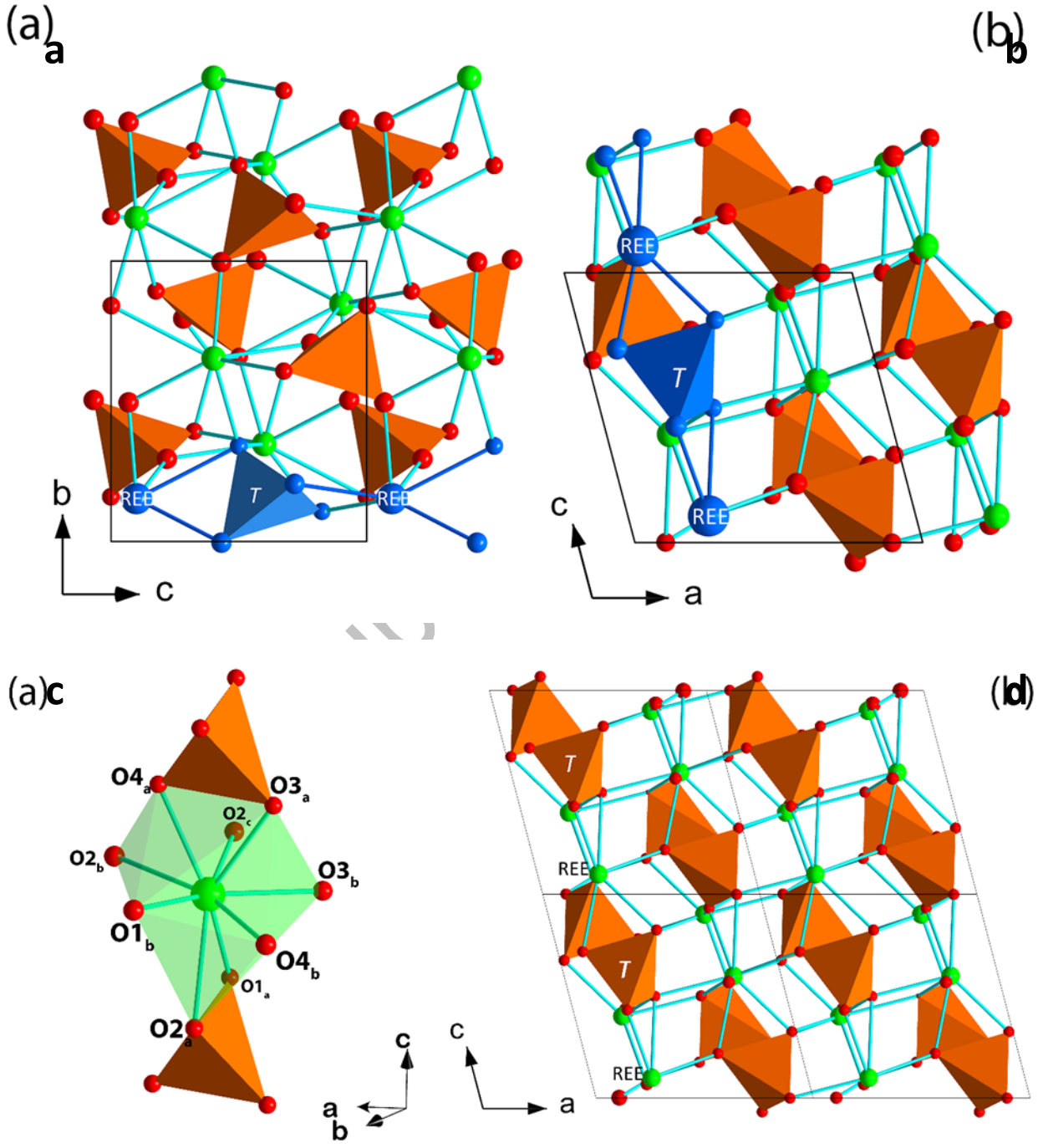

https://doi.org/10.1180/mgm.2024.70 Published online by Cambridge University Press

Fig. 4. High-pressure evolution of the unit-cell parameters (normalized to ambient conditions values) of (a) the investigated (Ca,Th)-poor and (b) (Ca,Th)-enriched chernovite-(Y) samples and (c) of their respective normalized unit-cell volumes with the refined Birch-Murnaghan equations of state. Empty symbols refer to data collected in decompression.

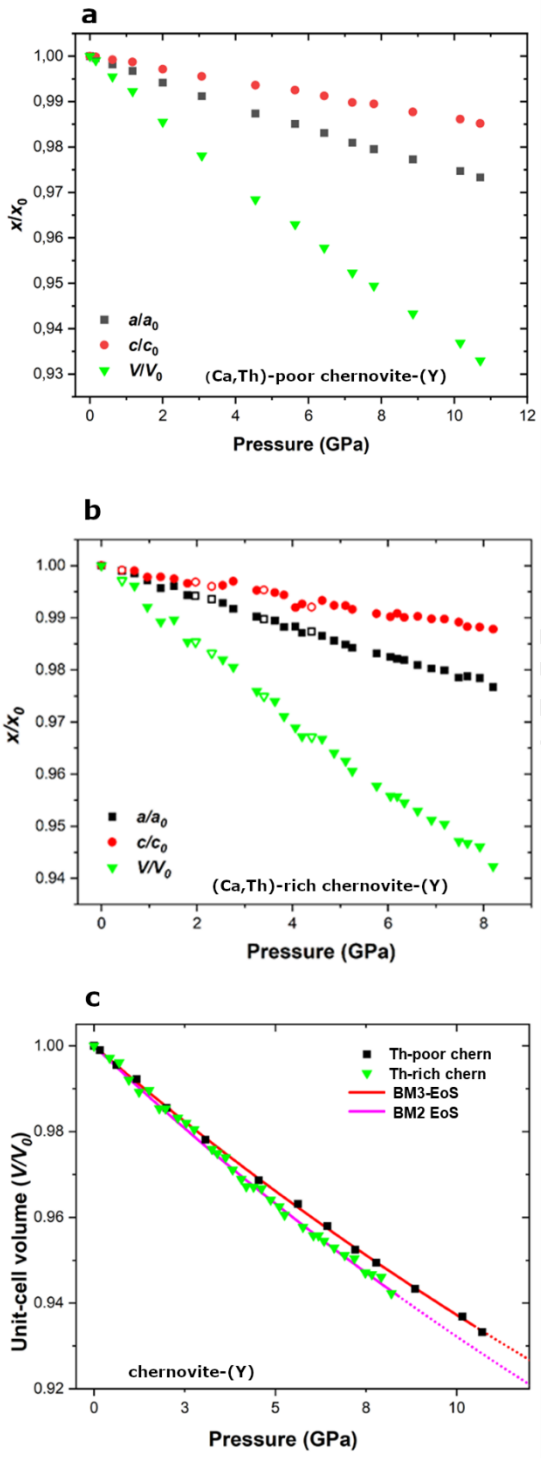

https://doi.org/10.1180/mgm.2024.70 Published online by Cambridge University Press

Fig. 5. High-pressure evolution of the unit-cell parameters (normalized to ambient-conditions values) of (a) xenotime-(Y) and (c) monazite-(Ce), (b) the normalized unit-cell volumes of the ambient-pressure and high-pressure polymorphs of xenotime-(Y) and (d) of the monoclinic *β* angle of monazite-(Ce).

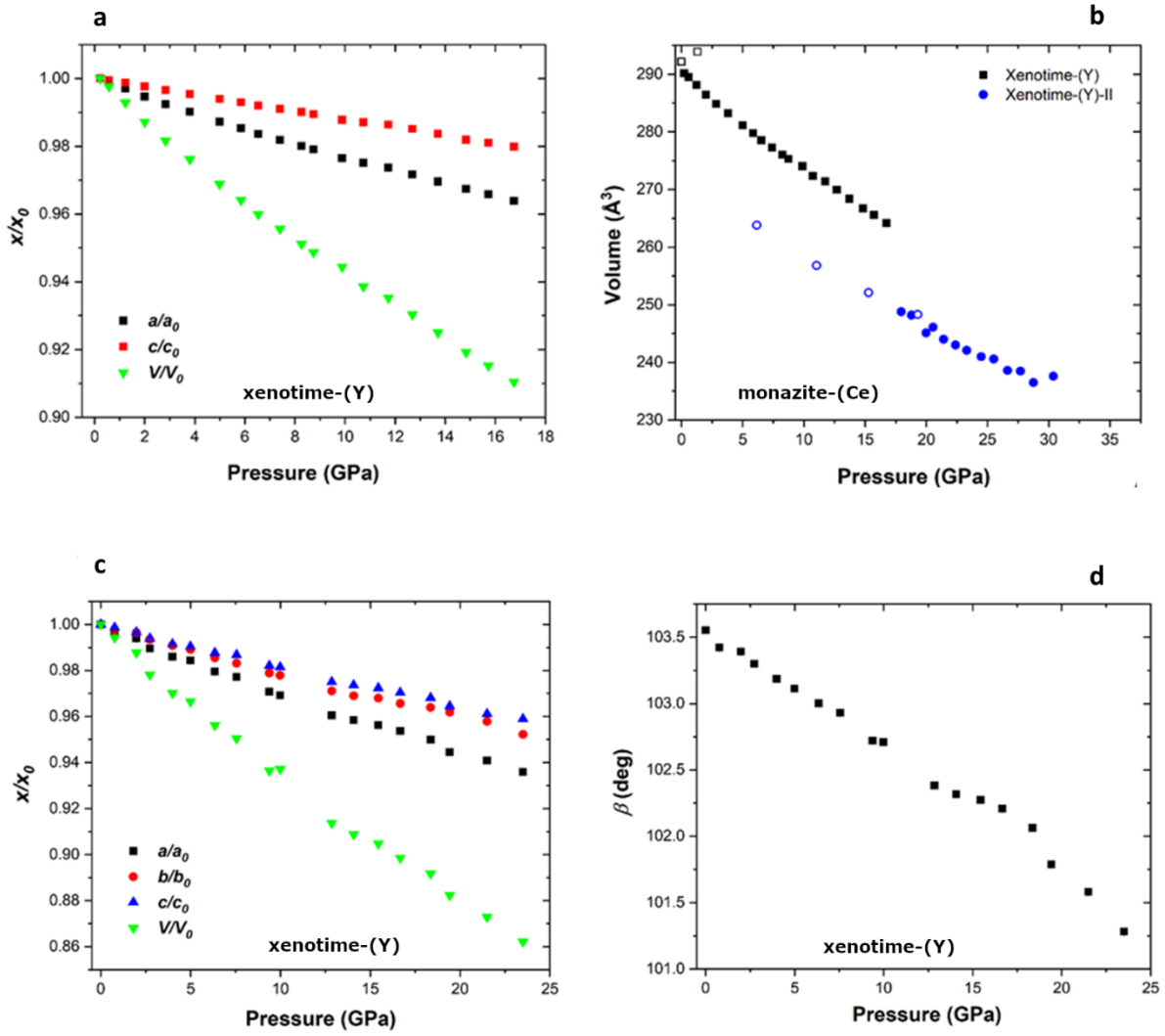

https://doi.org/10.1180/mgm.2024.70 Published online by Cambridge University Press

Fig. 6. High-temperature evolution of the unit-cell parameters (normalized to ambient-conditions values) of (a) (Ca,Th)-poor and (b) (Ca,Th)-enriched chernovite-(Y), (c) xenotime-(Y) and (d) monazite-(Ce).

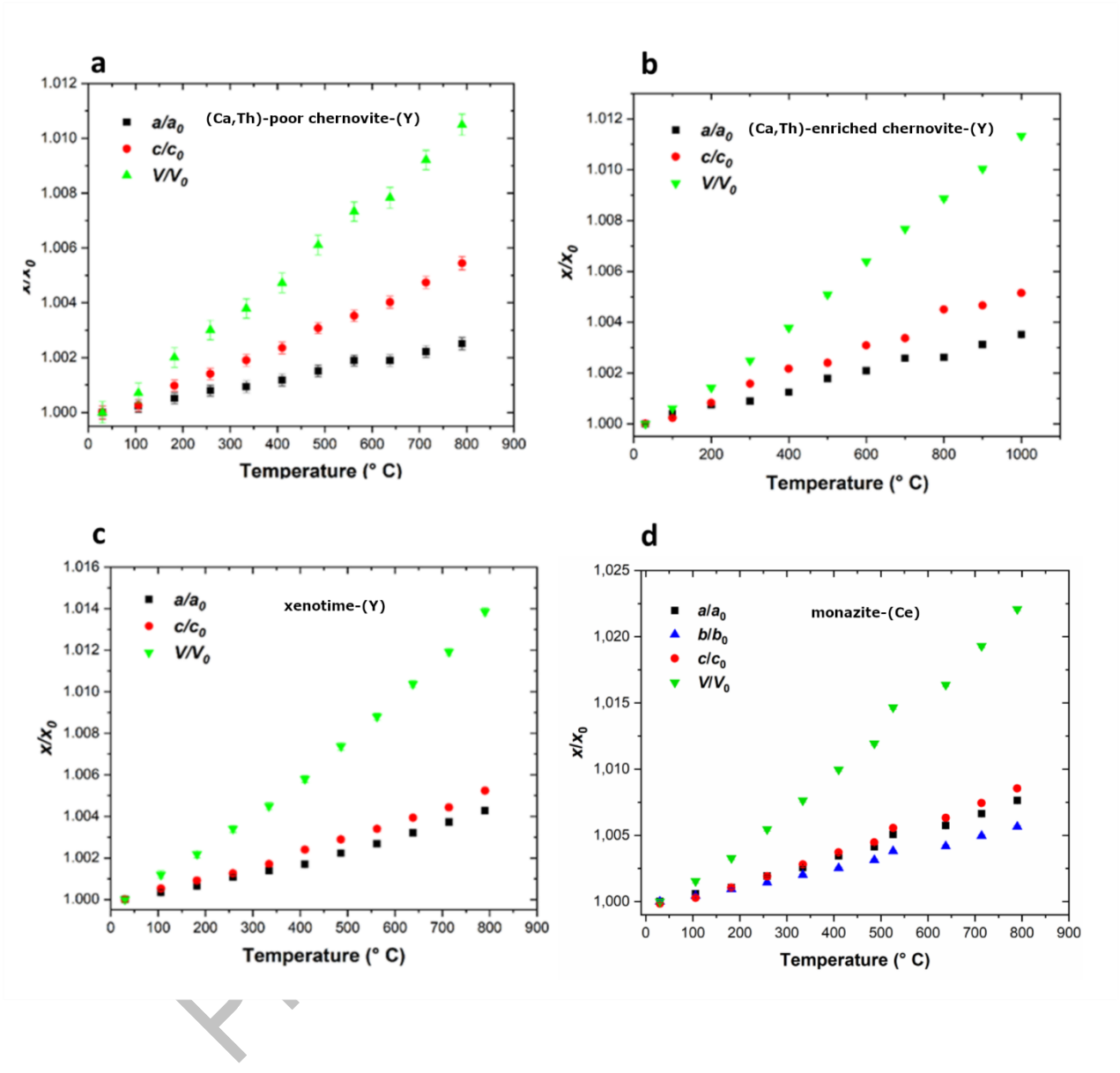

https://doi.org/10.1180/mgm.2024.70 Published online by Cambridge University Press

Fig. 7. (a) Bulk moduli as a function of the *A*-site atomic radii for several REETO_4 (*T*=As,P,V) minerals, after Li *et al.* (2009) and Zhang *et al*. (2008). (b) High-pressure evolution of the *A*-O interatomic bond distances in monazite-(Ce).

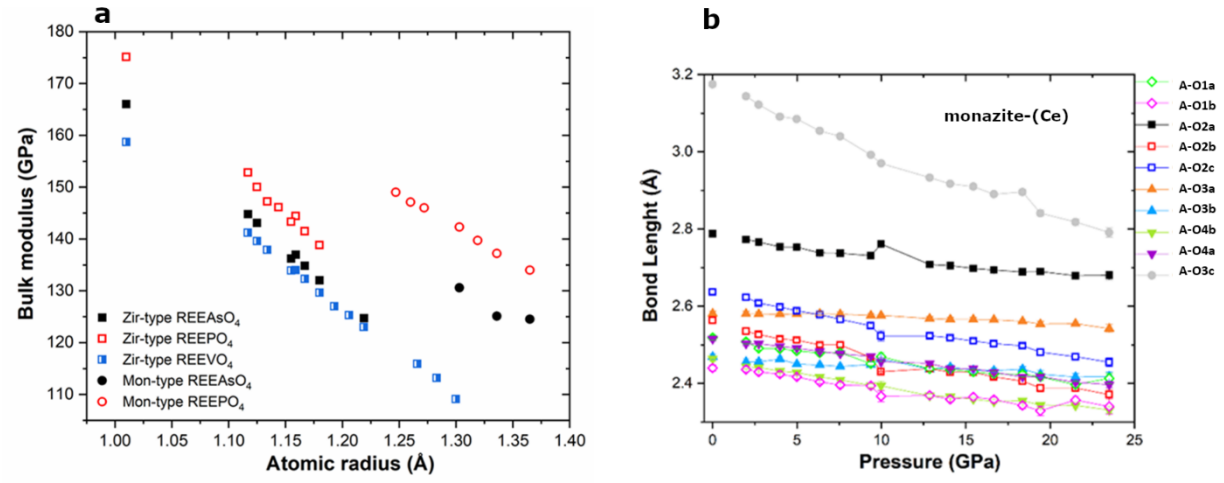

https://doi.org/10.1180/mgm.2024.70 Published online by Cambridge University Press

Table 1. Average (and range of the measured) chemical composition (expressed in oxide wt % and in atoms per formula unit (apfu) calculated on the basis of 4 oxygen atoms) of the chernovite-(Y), xenotime-(Y) and monazite-(Ce) samples under investigation.

	Chernovite-(Y)*		Chernovite-(Y)**		Xenotime-(Y)***		Monazite-(Ce)****	
As_2O_5	36.11	(34.77-36.91)	36.36	(30.95 – 42.80)	5.49	(3.45-6.81)	1.95	(1.36-2.84)
P_2O_5	5.41	(3.93-6.86)	2.30	(1.38 – 4.52)	28.7	(25.99-31.00)	27.71	(26.60-28.55)
SiO_2	0.82	(0.45-1.59)	2.40	(1.10 – 3.61)	0.34	(0-0.81)	0.24	(0.02-0.69)
V_2O_5	0.01	(0-0.05)	<0.01	(0 – 0.02)	b.d.l.		b.d.l.	
CaO	0.01	(0-0.03)	0.52	(0.03 – 1.26)	0.01	(0-0.06)	1.19	(0.54-1.59)
Y_2O_3	33.10	(29.91-35.38)	29.20	(25.94 – 31.94)	39.44	(37.11-41.55)	0.54	(0.39-0.62)
La_2O_3	0.01	(0-0.05)	0.05	(0 – 0.20)	0.03	(0-0.12)	14.18	(12.31-15.82)
Ce_2O_3	0.13	(0.01-0.25)	0.16	(0.07 – 0.26)	0.07	(0-0.20)	30.84	(28.41-32.95)
Pr_2O_3	0.04	(0-0.09)	0.05	(0 -0.13)	0.03	(0-0.18)	3.46	(3.09-3.93)
Nd_2O_3	0.37	(0.03-0.65)	0.57	(0.07 – 0.94)	0.26	(0.08-0.48)	12.88	(12.21-14.46)
Sm_2O_3	0.73	(0.55-1.06)	0.84	(0.26 – 1.60)	0.73	(0.43-1.04)	2.20	(1.86-2.45)
Eu_2O_3	b.d.l.		b.d.l.		b.d.l.		b.d.l.	
Gd_2O_3	2.30	(1.73-3.07)	3.02	(1.70 – 5.44)	3.84	(2.95-5.03)	1.41	(1.04-2.06)
Tb_2O_3	0.55	(0.39-0.60)	0.63	(0.40 0.86)	0.87	(0.68-1.07)	b.d.l.	

This is a 'preproof' accepted article for Mineralogical Magazine. This version may be subject to change during the production process.
DOI: 10.1180/mgm.2024.70

Dy_2O_3	5.10	(4.39-5.58)	4.51	(3.81 – 5.05)	6.23	(5.36-6.70)	0.27	(0.13-0.43)
Ho_2O_3	2.39	(2.09-2.78)	2.40	(1.87 – 3.44)	3.27	(2.65-4.14)	0.25	(0.10-0.44)
Er_2O_3	3.51	(2.98-4.24)	2.58	(1.76 – 3.73)	3.55	(3.13-4.13)	0.03	(0-0.22)
Tm_2O_3	0.48	(0.27-0.83)	0.37	(0 – 0.71)	0.46	(0-0.68)	0.07	(0-0.21)
Yb_2O_3	3.38	(1.87-5.07)	2.29	(1.24 – 4.58)	3.08	(2.34-3.71)	0.04	(0-0.39)
Lu_2O_3	1.29	(1.01-1.73)	1.06	(0.92 – 1.14)	1.56	(1.07-1.95)	0.07	(0-0.24)
PbO	0.26	(0.19-0.31)	0.16	(0 - 0.39)	0.25	(0.04-0.47)	0.03	(0-0.20)
ThO_2	2.40	(0.78-4.94)	7.32	(1.40 – 12.70)	1.89	(0.31-3.87)	2.55	(0.57-5.70)
UO_2	1.90	(1.26-2.32)	3.93	(3.95 – 4.27)	0.40	(0.01-0.74)	0.05	(0-0.17)
Tot.	100.41		100.84		100.62		100.05	
As	0.766		0.798		0.102		0.040	
P	0.185		0.081		0.861		0.934	
Si	0.033		0.101		0.012		0.009	
V	/		/		/		/	
Ca	/		0.023		/		0.051	
Y	0.714		0.652		0.744		0.011	
La	/		0.001		/		0.208	
Ce	0.001		0.002		/		0.449	
Pr	/		/		/		0.050	
Nd	0.005		0.008		0.003		0.183	
Sm	0.010		0.012		0.008		0.030	
Eu	/		/		/		/	

https://doi.org/10.1180/mgm.2024.70 Published online by Cambridge University Press

Gd	0.044		0.042		0.039		0.018	
Tb	0.007		0.008		0.010		/	
Dy	0.066		0.061		0.071		0.003	
Ho	0.030		0.032		0.036		0.003	
Er	0.022		0.034		0.015		/	
Tm	0.006		0.005		0.005		/	
Yb	0.042		0.029		0.033		/	
Lu	0.015		0.013		0.016		/	
Pb	0.002		0.001		0.002		/	
Th	0.022		0.070		0.015		0.023	
U	0.017		0.036		0.003		/	

*(Ca,Th)-poor chernovite in the text and Ch_{10} sample in Pagliaro *et al*. (2022a); **(Ca,Th)-enriched chernovite in the text and Ch_{13} in Pagliaro *et al*. (2022a); ***Xen_{14} sample in Pagliaro *et al*. (2022a); ****Mon_{14} sample in Pagliaro *et al*. (2022a)

https://doi.org/10.1180/mgm.2024.70 Published online by Cambridge University Press

Table 2. Details pertaining to the *in situ* high-pressure and high-temperature experiments of this study.

Experiment	Technique*	Wavelength (Å)	*P*-transmitting medium**	Maximum *P*/*T* (GPa/°C)	Detector type / Instrument model	Exposure time per frame (s)	Synchrotron beamline / Institution
High-pressure experiments							
(Ca,Th)-poor chernovite-(Y) at high-*P*	SC-XRD	0.41066	He	10.71(5)	Eiger2 9M CdTe	0.2	ID15B, ESRF
(Ca,Th)-enriched chernovite-(Y) at high-*P*	PXRD	0.29060	*m.e.w.*	8.20(5)	Perkin Elmer XRD1621	***	P02.2, Petra-III
Xenotime-(Y) at high-*P*	SC-XRD	0.41029	He	30.38(5)	Eiger2 9M CdTe	0.5	ID15B, ESRF

This is a 'preproof' accepted article for Mineralogical Magazine. This version may be subject to change during the production process.
DOI: 10.1180/mgm.2024.70

Monazite-(Ce) at high-*P*	SC-XRD	0.29060	Ne	23.50(5)	Perkin Elmer XRD1621	1	P02.2, Petra-III
High-temperature experiments							
(Ca,Th)-poor chernovite-(Y) at high-*T*	SC-XRD	0.71359	-	790(5)	Stoe IPDS II	5.5	IMP #
(Ca,Th)-enriched chernovite-(Y) at high-*T*	PXRD	0.7293	-	1000(5)	Scintillator	***	MCX, Elettra
Xenotime-(Y) at high-*T*	SC-XRD	0.71359	-	790(5)	Stoe IPDS II	2	IMP #
Monazite-(Ce) at high-*T*	SC-XRD	0.71359	-	790(5)	Stoe IPDS II	2	IMP #

* SC-XRD: single-crystal X-ray diffraction; PXRD: powder X-ray diffraction

** He: helium (Klotz et al., 2009); Ne: neon (Klotz et al., 2009); *m.e.w.*: methanol:ethanol:water = 16:3:1 (Angel et al., 2007)

*** See the text for further details

Institute of Mineralogy and Petrography, University of Innsbruck, Austria

https://doi.org/10.1180/mgm.2024.70 Published online by Cambridge University Press

Table 3. Refined equations of state parameters from the fit to the experimental high-pressure and high-temperature unit-cell volume data (see text for further details).

High-pressure experiments

	BM3 EoS				BM2 EoS		
	K_{V0} (GPa)	β_V (GPa^{-1})	K_V'	V_0 (Å^3)	K_{V0} (GPa)	β_V (GPa^{-1})	V_0 (Å^3)
(Ca,Th)-poor chernovite-(Y)	136(2)	0.0074(1)	4.0(5)	310.43(3)	135.5(5)	0.00738(1)	310.43(3)
(Ca,Th)-enriched chern.-(Y)	125(3)	0.0080(1)	3.8(9)	316.16(9)	123.8(9)	0.00808(7)	316.17(7)
Xenotime-(Y)	145(4)	0.0068(2)	4.4(5)	290.4(2)	148(1)	0.00676(5)	290.4(1)
Monazite-(Ce)	-	-	-	-	121(3)	0.0083(2)	299.3(4)
Gasparite-(Ce)*	109(4)	0.0092(3)	4.3(6)	320.6(3)	105(1)	0.00951(9)	320.7(2)

* From Pagliaro *et al*. (2022b)

High-temperature experiments

	Holland-Powell EoS				1st order polynomial fit	
	α_V (x10^{-6} K^{-1})	a_0 (x10^{-5} K^{-1})	a_1 (x10^{-4} K$^{-1/2}$)	V_0 (Å^3)	LTEC (x10^{-6} K^{-1})	V_0 (Å^3)
(Ca,Th)-poor chernovite-(Y)	9.7(1)	2.33(3)	0	307.02(3)	4.81	306.74
(Ca,Th)-enriched chern.-(Y)	8.0(1)	1.90(2)	0	313.06(2)	3.98	312.84
Xenotime-(Y)	9.6(12)	3.5(3)	0.8(4)	288.07(4)	6.00	287.73
Monazite-(Ce)	19.9(13)	4.9(3)	0.2(4)	297.97(5)	9.73	297.50

α_V: volume thermal expansion coefficient at ambient conditions calculated on the basis of the Holland-Powell EoS; a_0 and a_1 are two refinable variables in the Holland-Powell EoS (Holland and Powell, 1998)

This is a 'preproof' accepted article for Mineralogical Magazine. This version may be subject to change during the production process.
DOI: 10.1180/mgm.2024.70

Table 4. Refined equations of state parameters pertaining to the *A*- and *T*-sites coordination polyhedra from the high-pressure (BM2 EoS) and high-temperature (Holland-Powell EoS, only *A*-site coordination polyhedron) experiments.

High-pressure experiments

	$K_{V(AO8/AO9)}$ (GPa)	$V_{0(AO8/AO9)}$ (Å^3)	$K_{V(TO4)}$* (GPa)	$V_{0(TO4)}$ (Å^3)
(Ca,Th)-poor chernovite-(Y)	120(12)	23.53(9)	262(56)	2.319(10)
Xenotime-(Y)	126(4)	23.18(4)	299(62)	1.900(9)
Xenotime-(Y)-II	87(26)	30.4(12)	-	-
Monazite-(Ce)	110(4)	32.45(8)	395(130)	1.863(12)
Gasparite-(Ce)**	99(3)	33.02(4)	-	-

* Due to the high uncertainties, these data should be considered as a qualitative estimation of the TO_4 units rigid behaviour

** From Pagliaro *et al*. (2022b)

High-temperature experiments

	$\alpha_{V(AO8/AO9)}$ (x10^{-6} K^{-1})	a_0 (x10^{-5} K^{-1})	a_1 (x10^{-4} K$^{-1/2}$)	$V_{0(AO8/AO9)}$ (Å^3)
(Ca,Th)-poor chernovite-(Y)	16(3)	3.8(7)	0	23.49(4)
Xenotime-(Y)	18(2)	4.2(5)	0	23.03(4)
Monazite-(Ce)	25(2)	6.0(5)	0	32.36(4)

https://doi.org/10.1180/mgm.2024.70 Published online by Cambridge University Press